Materials & Design 208 (2021) 109921

Contents lists available at ScienceDirect

Materials & Design

journal homepage: www.elsevier.com/locate/matdes

Mechanical properties and microstructure of additively manufactured stainless steel with laser welded joints

Ruizhi Zhang [a,*], Craig Buchanan [a], Ville-Pekka Matilainen [b], Dafni Daskalaki-Mountanou [c], T. Ben Britton [c,d], Heidi Piili [b], Antti Salminen [e], Leroy Gardner [a]

[a] Department of Civil and Environmental Engineering, Imperial College London, London, UK
[b] Research Group of Laser Materials Processing, LUT University, Lappeenranta, Finland
[c] Department of Materials, Imperial College London, London, UK
[d] Department of Materials Engineering, University of British Columbia, London, Canada
[e] Department of Mechanical and Materials Engineering, University of Turku, Turku, Finland

HIGHLIGHTS

- Microstructural analysis reveals narrow weld regions and HAZ generated by employed laser welding.
- Anisotropy of additively manufactured base material and effects of energy input of laser welding are examined.
- Local and global stress-strain relationships are determined using non-contact digital image correlation method.
- Results of tensile tests on additively manufactured stainless steel coupons with laser welded joints are presented.
- Variations in the mechanical properties are correlated with differences in internal microstructure.

GRAPHICAL ABSTRACT

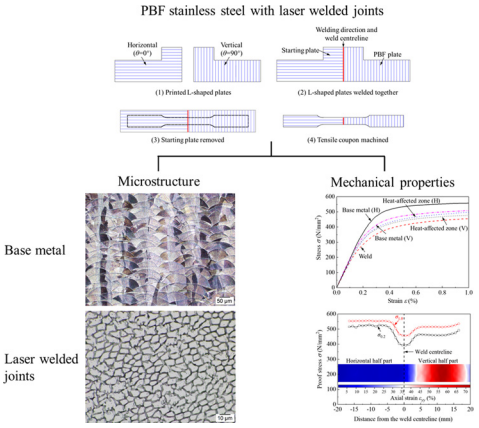

ARTICLE INFO

Article history:
Received 20 April 2021
Revised 4 June 2021
Accepted 18 June 2021
Available online 21 June 2021

Keywords:
316L stainless steel
Additive manufacturing (AM)
Digital image correlation (DIC)
Laser welding
Microstructure
Mechanical properties
Powder bed fusion (PBF)
Weldability

ABSTRACT

Powder bed fusion (PBF) is a commonly employed metal additive manufacturing (AM) process in which components are built, layer-by-layer, using metallic powder. The component size is limited by the internal build volume of the employed PBF AM equipment; the fabrication of components larger than this volume therefore requires mechanical joining methods, such as laser welding. There are, however, very limited test data on the mechanical performance of PBF metal with laser welded joints. In this study, the mechanical properties of PBF built 316L stainless steel parts, joined together using laser welding to form larger components, have been investigated; the microstructure of the components has also been examined. 33 PBF 316L stainless steel tensile coupons, with central laser welds, welded using a range of welding parameters, and with coupon half parts built in two different orientations, were tested. The porosity, microhardness and microstructure of the welded coupons, along with the widths of the weld and heat-affected zone (HAZ), were characterised. The PBF base metal exhibited a typical cellular microstructure, while the weld consisted of equiaxed, columnar and cellular dendrite microstructures. Narrow weld regions and HAZs were observed. The PBF base metal was found to have higher proof and ultimate strengths, but a similar fracture strain and a lower Young's modulus, compared with

* Corresponding author.
E-mail address: r.zhang18@imperial.ac.uk (R. Zhang).

https://doi.org/10.1016/j.matdes.2021.109921

conventionally manufactured 316L stainless steel. The strengths were dependent on the build direction – the vertically built specimens showed lower proof strengths than the horizontal specimens. The laser welds generally exhibited lower microhardness, proof strengths and fracture strains than the PBF base metal which correlated with the observed structure. This work has demonstrated that PBF built parts can be joined by laser welding to form larger components and provided insight into the resulting strength and ductility.

1. Introduction

Additive manufacturing (AM), commonly known as 3D printing, is a family of novel manufacturing techniques in which material is added layer-by-layer to build objects based on 3D model data [1]. In recent years, AM methods have become increasingly adopted in many industries, such as aerospace and biomedical [2–4], due to their ability to produce complex functional components with high precision, reduced material waste, minimised assembly processes and reduced tooling costs [2–4]. Modern AM techniques were first developed in the 1950s [5] and the following decades saw the development of the feedstock materials and commercially available manufacturing systems. AM techniques are today classified into seven categories by EN ISO/ASTM 52900 [1]: binder jetting, directed energy deposition, material extrusion, material jetting, powder bed fusion, sheet lamination and vat photopolymerization.

1.1. Metal additive manufacturing

EN ISO/ASTM 52900 [1] defines three fundamental metallic AM process categories: sheet lamination, directed energy deposition (DED) and powder bed fusion (PBF), with the two latter techniques being considered as the most suitable for use in the construction sector [6–9]. Sheet lamination is a process where layers of sheet material are cut and bonded together to form the final object. DED is the process of depositing molten metallic powder or wire to produce the final component; wire and arc additive manufacturing (WAAM) is an example of DED that is being actively explored for use in the construction sector [8]. PBF involves melting metallic powder within a powder bed to form the final three-dimensional component layer-by-layer, and is referred to by equipment manufacturers using a range of terms including: selective laser melting, electron beam melting, direct metal laser sintering and selective laser sintering [9,10]. The typical PBF process has been described previously [4,9,11], and is shown in Fig. 1. The process involves drawing the part in CAD software, converting to an STL model and slicing into individual two-dimensional layers to be printed. For manufacture, a thin layer of powdered material is then deposited, melted and solidified into a cross-section, the platform is lowered by the layer thickness and the manufacturing process repeats until completion. The finished part is finally removed from the build plate. During the PBF building process, a laser or electron beam is programmed to deliver the necessary thermal energy to melt the deposited metallic powder. The final part experiences many repeated heating and cooling cycles, with repeated phase transformation between solid and liquid states until the part is completed; this can result in a very different microstructure and mechanical properties when compared with conventionally manufactured material [2,8].

To date, many studies have focused on the microstructural features and mechanical properties of PBF additive manufactured metallic materials, including titanium alloys [2,3], aluminium alloys [3,12,13], nickel alloys [14–16] and stainless steels [3,4,17–36]. PBF 316L stainless steel has been the focus of a number of prior studies due to its high strength, corrosion resistance and good weldability characteristics [19,36]. These studies have explored the microstructural characteristics, with a typical cellular [19–24] or cellular-dendritic [17,25,31] microstructure observed. The material characteristics of PBF 316L stainless steel have also been investigated, through its porosity [32–34], hardness [22,25,29,35], tensile properties [20,24–27], surface roughness [28–30], fatigue properties [2,23] and corrosion resistance [19]. Porosity was reported to have a detrimental influence on the mechanical response, with high-porosity PBF specimens exhibiting a premature brittle failure with limited necking [32,33]. The microhardness of PBF 316L stainless steel has been found to be similar in value regardless of the build direction [29] and higher compared with that of its annealed conventional counterparts [35], due to finer grain sizes arising through the PBF building process. PBF 316L parts have been shown to have higher proof and ultimate

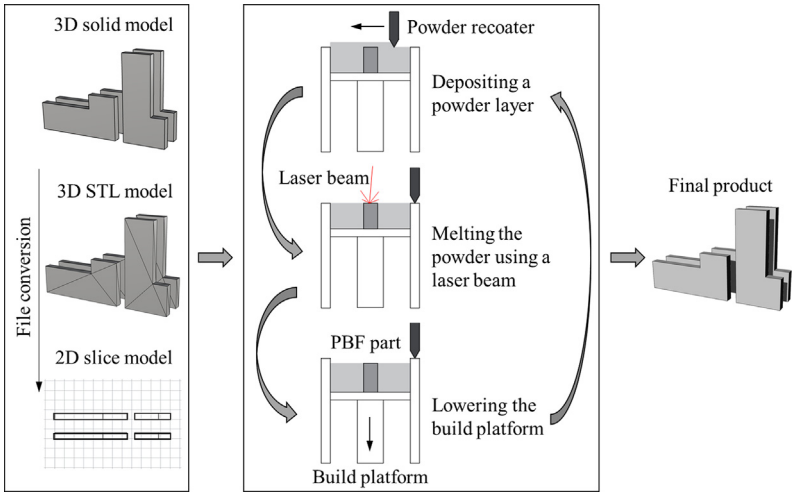

Fig. 1. Overview of the powder bed fusion (PBF) process.

strengths, without reduced ductility despite the presence of pores, in comparison to conventionally produced 316L stainless steel, where reduced ductility is typically seen with higher strength [18,21–23]. The higher strengths have been associated with the formation of a finer microstructure and a higher density of dislocations, achieved as a result of the rapid cooling inherent in the PBF process [18,23,25]. It is well established that PBF parts can exhibit strongly anisotropic mechanical properties; this is attributed to the presence of lack-of-fusion defects [3,20,24,32], the crystallographic texture [8] and the presence of elongated grains with epitaxial growth parallel to the build direction [17,20,26].

Although AM has many advantages over conventional manufacturing, applications in certain industries, including construction, remain limited due to its long build time and limited single part dimensions, particularly for the aforementioned metallic PBF. Currently the build time for metallic PBF is lengthy with individual layers having typical thicknesses of the order of 10^1 μm [4]. The maximum part size is limited by the build envelope of the printing machine, which is up to roughly 1000 × 1000 × 500 mm^3 at present for metallic PBF [37]. The as-built parts additionally have an inherent rough surface texture from the manufacturing process, which may require post processing for some applications. Studies into the structural applications of PBF metallic elements have explored square and circular hollow section (SHS and CHS) compression elements [4,11], cellular lattice structures [38–40], honeycomb-like structures with a negative Poisson's ratio [41,42] and structural connection nodes [43].

1.2. Laser welded joints

The requirement for large-scale metallic components, particularly in the construction industry, necessitates joining smaller, individually built, PBF parts together [44]. Conventional welding techniques, such as gas tungsten arc welding [45], gas metal arc welding [46] and resistance spot welding [36,47], have been extensively utilised in the industry to mechanically join small conventionally produced metallic pieces together. Laser welding is an alternative mechanical joining process that results in narrower welds and heat-affected zones (HAZ), reduced thermal distortions to the surrounding base material and lower residual stresses than the aforementioned conventional welding techniques [48–51]. All welding processes, however, can induce local changes in the microstructure, leading to different mechanical properties and corrosion resistance from the original base material [52].

Conventionally formed 316L stainless steel with laser welded joints has been previously studied in terms of microstructure [49,53–55], microhardness [49,53,54], creep rupture [49] and mechanical properties [52–54], as well as dissimilar laser welding of conventional 316L stainless steel to other alloys, such as brass [56] and titanium alloys [57,58]. Various microstructures for laser welds in conventional 316L stainless steel have been observed, such as cellular and equiaxed dendritic structures [49] and cellular dendritic structures [53,55], related to various cooling rates and G/R ratios (G is temperature gradient and R is growth rate) of the laser welding [49,53]. Coarsening grains, or the occurrence of dendrites, in welds with high heat input have been found to reduce the mechanical properties of the welded joints [53]. The mechanical properties within the weld region have been observed to be different to those measured from the base metal [48]. A common technique for the measurement of the local stress-strain response across welds, is full field non-contact digital image correlation (DIC) [52,59–62], which tracks random patterns applied to the specimen surface and is later processed to calculate the surface strain field.

The microhardness [44], weld geometry [44,48], microstructure [44,63] and mechanical properties [44,63] in laser welded similar and dissimilar parts of PBF 316L stainless steel have also been investigated, although only with the individual PBF parts built in the same orientation. In these studies [44,63], the laser welds were found to have a cellular and columnar dendritic microstructure with random grain orientations, no porosity and lower microhardness and tensile properties than the base material. Other studies have investigated the microstructure and mechanical properties of PBF titanium alloys with gas tungsten arc welding [64], PBF Ti-6Al-4V parts with laser welding [65], PBF AlSi10Mg parts with laser and tungsten inert gas welded joints [66], PBF titanium alloy with electron beam welds [67] and PBF 304 stainless steel with laser welding [68]. However, there is little research in the literature on the correlation between the microstructure and mechanical properties of PBF 316L stainless steel parts with laser welded joints, with no prior consideration of joints between parts with different build orientations.

The joining of small PBF 316L stainless steel parts, to produce larger components, using laser welding, is explored in the present paper. Microstructure, microhardness and tensile coupon tests on parts printed in different build directions and laser welded together, with varying welding parameters, are described. DIC techniques have been used to provide detailed insight into the extent and mechanical properties of the weld, HAZ and base material. The study provides new knowledge about the weldability of PBF stainless steel elements for use in the construction industry.

2. Specimen manufacture and preparation

The manufacture and preparation of the test specimens involved: (i) specimen building, (ii) laser welding and (iii) preparation for the microstructural observations and mechanical testing (discussed in Section 3); these three steps are outlined in this section. The feedstock material used in this study was Grade 316L austenitic stainless steel powder, with an average particle size between 15 μm and 53 μm [69]. The chemical composition and as-built mechanical properties of the PBF base material provided in the manufacturer's datasheet [69] are reported in Tables 1 and 2, respectively.

2.1. PBF specimen manufacture

A total of 66 L-shaped plates were manufactured using a modified research machine, based on an EOS M280 system, in the Laboratory of Laser Processing of the School of Energy Systems at LUT University. This system utilises an ytterbium continuous wave fibre laser within a build chamber filled with protective inert nitrogen. A schematic view of the powder bed fusion process is shown in Fig. 1. All PBF plates were printed simultaneously with identical processing parameters on the same build platform. The parameters used were: a laser power of 200 W, a scanning speed of 1000 mm/s, a laser spot size of 100 μm, a layer thickness of 20 μm, a hatch distance of 100 μm and a scan angle of 45° between successive layers. The scanning strategy is illustrated in Fig. 2, where the laser scanning directions are indicated by the arrows. The L-shaped plates were removed from the build plate and no additional surface treatment was applied.

The orientation of the printed L-shaped plates, and the later coupon half parts cut from these plates, with respect to the build direction, recoating direction and final loading direction, is shown in Fig. 3, where θ is the angle from the longitudinal axis of the coupon to the build plane (the xy plane). The L-shaped plates, and coupon half parts, were built either horizontally ($\theta = 0°$) and loaded parallel to the build plane, or vertically ($\theta = 90°$) and loaded normal to the build plane.

Table 1
Chemical composition of the 316L stainless steel feedstock powder from the manufacturer's datasheet [69].

Cr (%)	Ni (%)	Mo (%)	C (%)	Mn (%)	Cu (%)	P (%)	S (%)	Si (%)	N (%)	Fe (%)
17–19	13–15	2.25–3	≤0.03	≤2	≤0.5	≤0.025	≤0.01	≤0.75	≤0.1	Balance

Table 2
Mechanical properties of as-built 316L stainless steel parts from the manufacturer's datasheet [69].

Build direction angle (°)	Young's modulus (N/mm^2)	Yield strength (N/mm^2)	Ultimate tensile strength (N/mm^2)	Elongation at fracture (%)	Hardness (HRB)
0	185,000	470–590	590–690	25–55	89
90	180,000	380–560	485–595	30–70	89

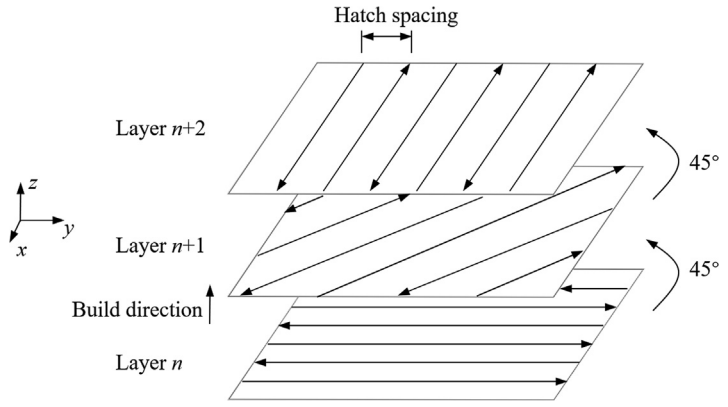

Fig. 2. Schematic of the laser scanning strategy used in the PBF process.

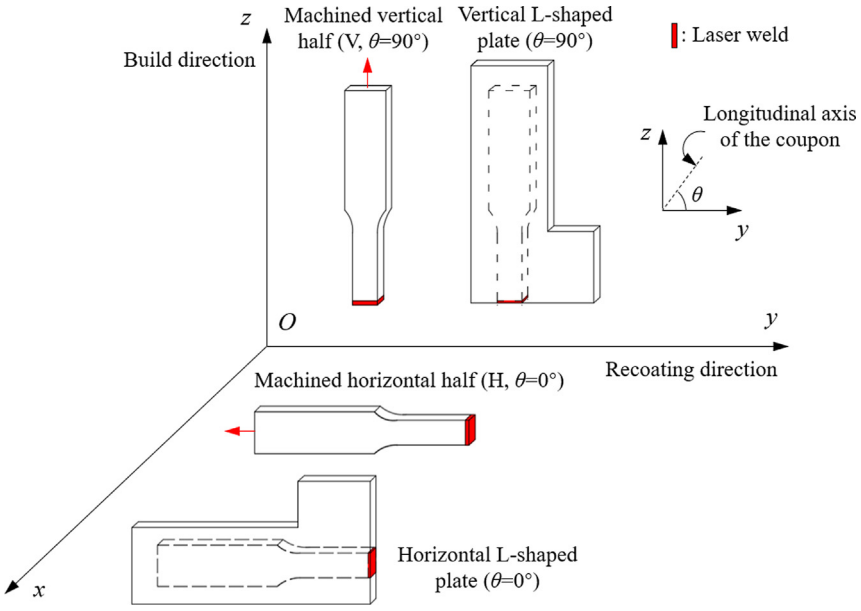

Fig. 3. Orientation of L-shaped plates and machined coupon half parts relative to the build plane (the *xy* plane).

2.2. Laser welding

The L-shaped plates were joined by laser welding in the following combinations: (i) horizontal (H, θ = 0° only), (ii) vertical (V, θ = 90° only) and (iii) combined horizontal and vertical (X, with one half being built horizontally θ = 0° and the other half being built vertically θ = 90°). Starting plates were used to initiate the laser welds; the welds then proceeded from the starting plates onto the PBF specimens. After welding, the starting plates were removed by sawing, and the tensile coupons were machined from the remaining welded plates. This process is shown in Fig. 4 for a combined X family coupon. The three coupon families produced

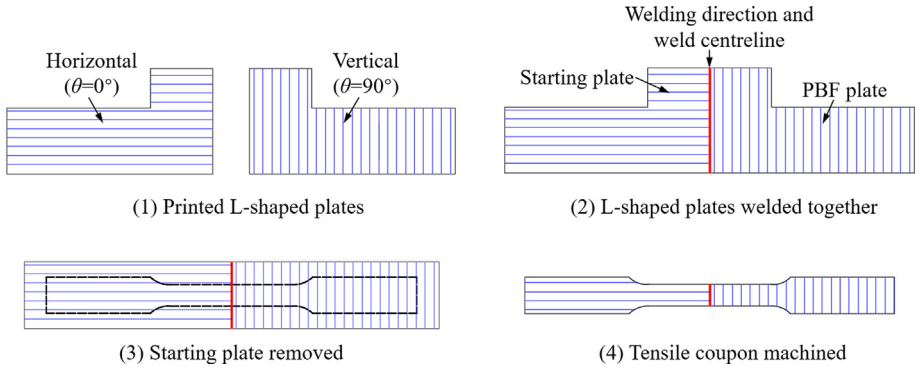

Fig. 4. Laser welding and machining process for a combined X family tensile coupon.

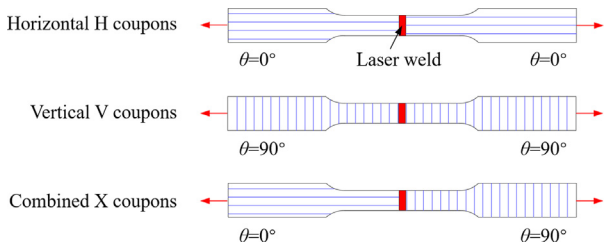

Fig. 5. Welded tensile coupon families, showing the print layer direction of the half parts.

Table 3
Adopted laser welding parameter sets for the welded tensile coupon families.

Welding parameter set	Laser power (W)	Welding speed (mm/s)	Energy input (J/mm)	Optical diameter (μm)
1	3500	29.2	120	300
2*	3500	33.3	105	300
3	4000	29.2	137	300
4	4000	33.3	120	300

* Welding parameter set 2 was not used for the combined X family coupons.

(H, V and X) are shown in Fig. 5. The laser welder had an optical fibre diameter of 300 μm. Two variations of welding power (P = 3500 W or 4000 W) and welding speed (S = 29.2 mm/s or 33.3 mm/s) were employed, as presented in Table 3. The heat input per unit length travelled by the laser beam E is calculated using Eq. (1),

$$E = \frac{P}{S}, \tag{1}$$

where E is the energy input, P is the laser power and S is the welding speed. The nominal geometry of the final test specimens was in accordance with EN ISO 6892-1 [70], and is shown in Fig. 6.

The test specimens were labelled beginning with the letter of the welded coupon family (H, V or X), followed by the welding parameter set from Table 3 (1, 2, 3 or 4) and finally the specimen repeat number (1, 2 or 3). For example, V1/3 denotes a vertical coupon (V) welded using welding parameter set 1, and the coupon is the third repeat (/3) in the V1 family. Three coupons were tested for each combination of coupon family and welding parameter set, with the exception that welding parameter set 2 was not used for the combined X family coupons, resulting in a total of 33 coupons.

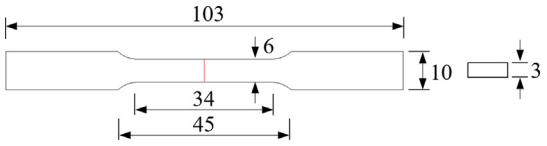

Fig. 6. Dimensions of welded tensile coupons (dimensions in mm).

3. Experimentation

PBF built parts experience a complex thermal history during their manufacturing process; this is known to influence both the microstructure and resulting mechanical properties [2,8]. The focus of the present study is on characterising the mechanical properties of laser welded PBF stainless steel parts through destructive tensile coupon tests, but a preliminary analysis linking the mechanical performance to the underlying microstructure is also presented. Optical microscopy (OM) observations, Vickers microhardness tests, tensile coupon tests and scanning electron microscopy (SEM) analysis were sequentially carried out. The OM analysis and microhardness tests were performed in the Engineering Alloys Lab, while the SEM analysis were conducted at the Harvey Flower Electron Microscopy Suite, both in the Department of Materials at Imperial College London. The tensile coupon tests were conducted in the Structures Laboratory of the Department of Civil and Environmental Engineering at Imperial College London.

3.1. Microstructural analysis

Prior to the destructive tensile coupon tests, a total of nine samples, listed in Table 4, with varying build orientations, laser power and scanning speeds, were selected from the specimen pool, and prepared for microstructural observations in accordance with ASTM E3-11 [71]. One face of each sample was ground with silicon carbide paper (increasing from 500, 800, 1200 to 2000 grit size) and polished to a mirror finish, using 3 μm and 1 μm diamond suspensions and finally a 0.04 μm diluted colloidal silica solution. The as-polished surfaces were observed using an Olympus BX51 optical microscope and analysed using the image processing software ImageJ [72] to calculate the porosity of the examined surface. In

Table 4
Tensile coupons selected for microstructural observations and microhardness tests.

Coupon type	Optical microscopy and microhardness tests			SEM and EBSD
Horizonal	H1/3	H2/3	H3/1	H1/1
Vertical	V1/2	V2/2	V3/1	–
Combined	X1/3	X3/3	X4/1	–

order to reveal the material microstructure, aqua regia and Kalling's No. 2 solutions, which were previously used by others for PBF 316L microsamples [25,73], were first employed as the chemical etchants, but were found to be not effective for the large dimension samples. The sample surfaces were instead successfully electrolytically etched using an oxalic acid solution, at 6 V for 60 s as recommended by ASTM E407-07 [74], and then ultrasonically cleaned in acetone to remove any residual reagents.

3.2. Microhardness tests

Microhardness measurements were carried out on the as-etched specimens, in compliance with ISO 6507–1 [75], using a Zwick/Roell ZHV Vickers hardness tester equipped with an optical microscope. An applied load of 0.98 N, with a dwell time of 10 s, was used for all indentations. To evaluate the variation of the microhardness in the weld, HAZ and base metal, indentations were made along the parallel length of the tensile coupons, at the locations shown in Fig. 7(a). Working along the longitudinal coupon axis, indentations were made at 0.5 mm intervals for the base metal and 0.1 mm intervals for the weld and expected HAZs, to measure the microhardness profile along the coupon. Average values of the microhardness for these three regions were calculated by taking measurements in the transverse direction, at 0.5 mm intervals, along the weld centre, within the HAZ and for the base metal away from the HAZ (Fig. 7(b)).

3.3. Tensile coupon tests

Tensile coupon tests were undertaken to evaluate the strength of the laser welded joints in line with EN ISO 6892-1 [70] using an Instron 8802 testing machine, as shown in Fig. 8. The dimensions of the coupons were measured using digital callipers. A series of standard gauge lengths ($5.65\sqrt{S_0}$, where S_0 is the original cross-sectional area of the parallel length of the coupons) were scribed onto the front and back faces for post-test calculation of the fracture strain. A four-camera LaVision DIC system [76] was employed to measure strains over the parallel length on both coupon surfaces, with two cameras observing each side. The front and back faces of the coupons were spray painted white and a random black speckle pattern was applied to create trackable features along the parallel length. The testing machine was operated under displacement control; two crosshead separation rates were used – a rate of 0.00238 mm/s and 0.0085 mm/s prior to and after yielding respectively, with a gradual transition between the two rates, as recommended in EN ISO 6892–1 [70]. The applied load was measured using a load cell within the testing machine and recorded via an analogue to digital converter within the DIC system. The frequency for capturing the DIC images and loading data, was set to 1 Hz. The surface deformations and strains were obtained using the captured images in DaVis 8 [76]. In order to calculate the global strain from DIC measurements which is consistent with the tensile strain defined in EN ISO 6892-1 [70] using an extensometer, the global longitudinal strain was derived by averaging the strains over the full area of a gauge length within the parallel length on both faces for each coupon. The local longitudinal strains were also extracted from 1 mm long rectangular boxes, each covering the full width of the coupons, in order to show the strain variation along the parallel length of the welded coupon.

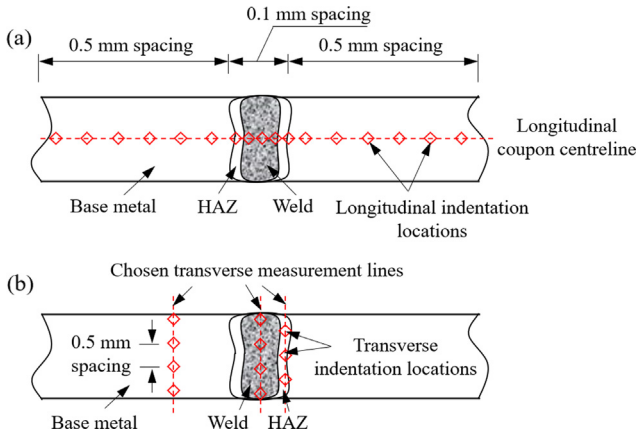

Fig. 7. Microhardness measurement locations for the weld, HAZ and base metal, showing indentation positions and intervals in the (a) longitudinal and (b) transverse directions (not to scale).

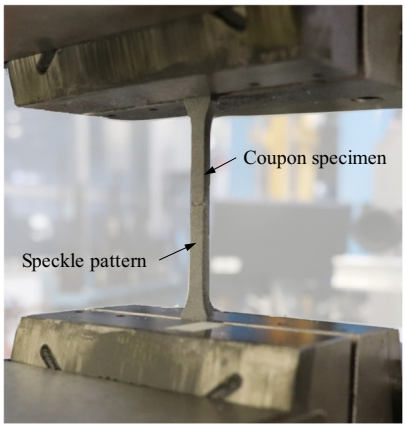

Fig. 8. Tensile coupon test setup.

3.4. Electron backscatter diffraction (EBSD) characterisation

Electron backscatter diffraction (EBSD) characterisation was performed after the conclusion of the tensile tests to examine the underlying grain structure further. The H1/1 specimen was sectioned into small metallographic pieces, and subsamples were extracted from the gripped region of the coupon. These were ground, polished, chemically etched using aqua regia and then examined using a Quanta Field Emission Gun (FEG) 650 scanning electron microscope equipped with a Bruker *e*-Flash HD and Esprit 2.1. The system was operated at 20 kV with the H1/1 subsamples tilted to 70° relative to the horizontal in the microscope.

4. Results and discussion

4.1. Porosity

Representative optical micrographs of as-polished horizontal and vertical base metal samples are presented in Fig. 9, where the process-induced and gas-induced pores are clearly visible. The gas-induced pores, highlighted in Fig. 9(a), had a spherical morphology that is consistent with the use of powder feedstock and were found to be nonuniformly distributed. A small fraction of processed-induced pores with irregular shapes, formed due to lack of fusion, as shown in Fig. 9(b). The area fraction of pores was calculated using ImageJ [72] and the results showed that the porosity was less than 0.5% in the PBF base metal. Additionally there was no significant difference in porosity between the examined surfaces of the horizontal and vertical samples, which is consistent with previous research [77]. Previous studies have reported that the porosity decreases with an increase in laser power and a

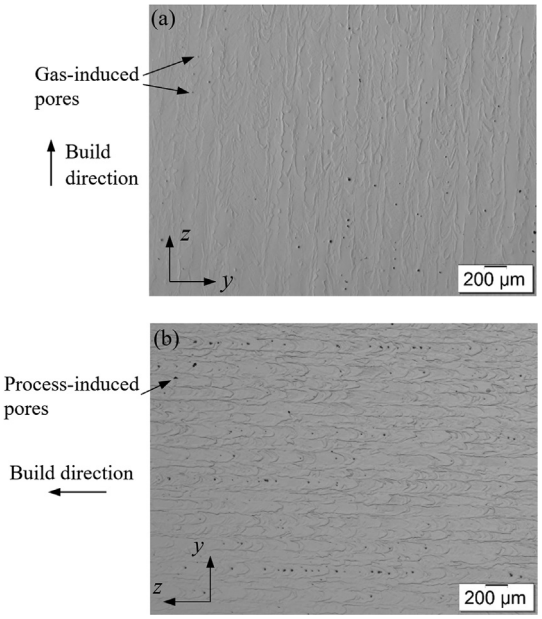

Fig. 9. Typical micrographs of an as-polished (a) horizontal coupon (H1/1) and (b) vertical coupon (V3/1).

reduction in scanning speed [28,33,78]. Although it was challenging to observe the weld boundaries prior to etching, the weld regions were seen to be almost pore-free, which was expected since the weld was formed with both a higher laser power and slower welding speed than those used in the PBF manufacturing process.

4.2. Microstructure characterisation

The microstructural features of the nine selected specimens were examined using OM and EBSD analysis. The examined surface was parallel to the build direction, covering multiple print layers, and is shown as the *yz* plane in Fig. 3. The microstructure of the chosen specimens, for both the PBF base metal and weld region, is described in this sub-section.

4.2.1. Microstructure of the PBF base metal

Figs. 10 and 11 depict typical optical micrographs of the PBF base metal for as-etched horizontal and vertical specimens, respectively, where the build direction is labelled, the red dashed lines denote the melt pool boundaries, the blue arrows indicate the grain orientations and the blue dashed lines show the grain boundaries. Periodic melt pools were revealed after electrolytic etching. At high magnification (Fig. 10(b) and Fig. 11(b)), the melt pools were observed to have half ellipse shapes, with a depth and width of approximately 60 μm and 120 μm respectively, and their size correlated with the heat input and laser spot diameter [79]. Overlapping scan areas of melt pools were observed between the adjacent PBF laser scan tracks and layers, indicating that partial remelting occurred (see Figs. 10-12). Smaller hatch distance and layer thickness employed for the printing, when compared with the measured width and depth of melt pools, led to larger overlapping degrees of laser-remelted traces, as illustrated in Fig. 12.

The PBF 316L base metal exhibited a typical cellular microstructure, which is consistent with previous observations on PBF 316L stainless steel [19–24], and was formed due to the very high cooling rates, of the order of 10^3-10^8 K/s [24], encountered in the manufacturing process. Epitaxial grain growth occurred during remelting, spanning over the melt pools within a layer and across multiple layers. Large elongated grains formed with a preferential orientation aligned with the build direction, close to the direction

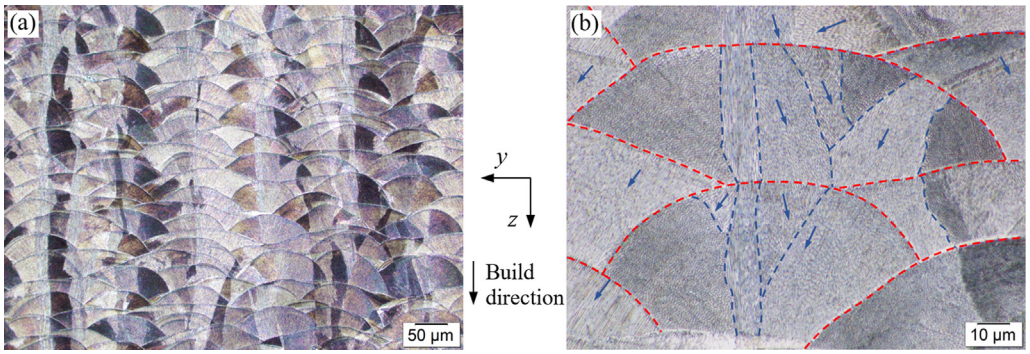

Fig. 10. Typical micrographs for an as-etched horizontal specimen (H1/3) for the (a) base metal and (b) melt pools.

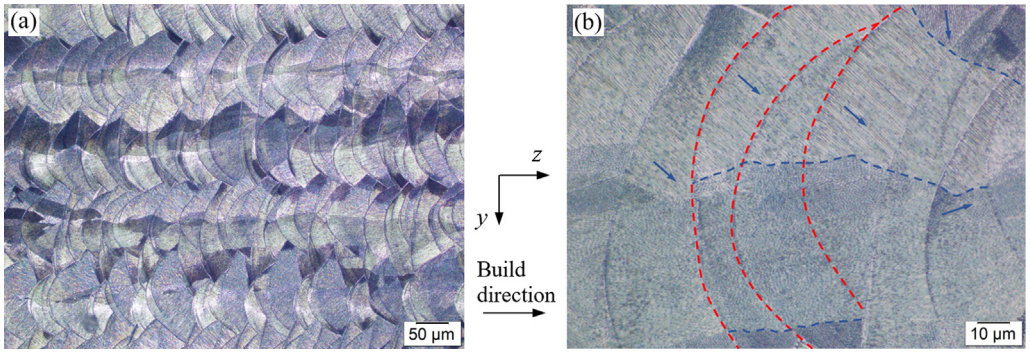

Fig. 11. Typical micrographs for an as-etched vertical specimen (V1/2) for the (a) base metal and (b) melt pools.

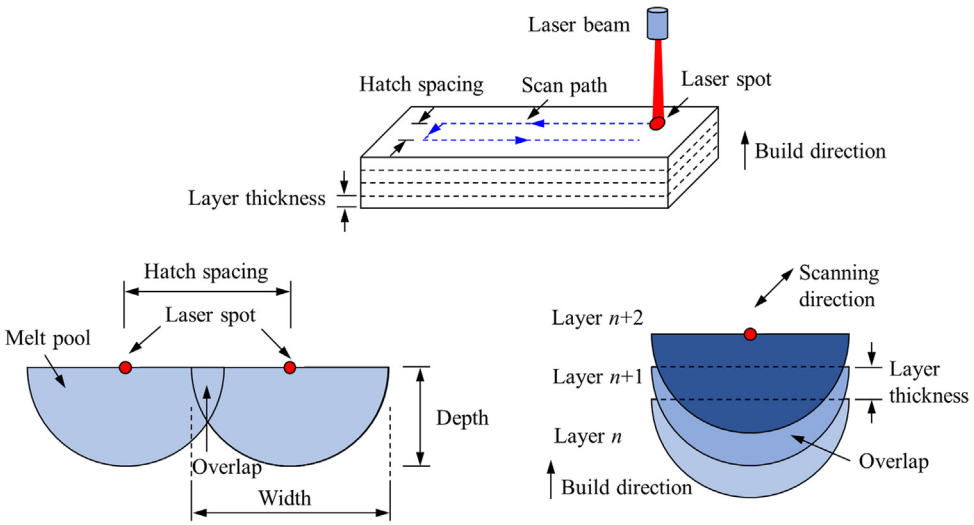

Fig. 12. Formation of scan tracks and partial remelting.

of the maximum thermal gradient. Small grains within the melt pools formed with no preferential growth orientation, resulting from nondirectional heat flow [25,26,44].

4.2.2. EBSD analysis of the PBF base metal

Forescatter diode (FSD) imaging was used on the EBSD detector to highlight regions of interest for microstructural characterisation during the EBSD analysis. Fig. 13 shows a typical FSD image taken from an as-etched horizontal subsample (extracted from H1/1), along with the corresponding inverse pole figure (IPF) map, where the colours correspond to the crystal orientations. The solidification characteristics of the PBF 316L base metal can be seen, with a typical cellular morphology and fully austenitic grains, which is consistent with that observed from the earlier OM analysis in Section 4.2.1. The columnar grains exhibited epitaxial growth, parallel to the build direction, and had a maximum size of 200 μm (Fig. 13 (b)), while small grains within the melt pools showed a random crystal orientation. The grains had an average size of about 28 μm, and the smallest detected grain size was 1 μm. Typical {100}, {101} and {111} pole figures of the examined surface are shown in Fig. 13(c), where the centre of each pole figure corresponds to the normal of the examined surface, and the scale bar shows the texture intensity of specific crystal orientation distributions. The high localised intensities on the pole figures represent the preferred orientations of the grain's pole, meaning certain families of grains are aligned in a crystallographic order. According to the {100} and {111} pole figures, a higher proportion of grains had a normal direction close to the ⟨100⟩ and ⟨111⟩ directions, but overall, the material exhibited a weak crystallographic texture, which is in line with other studies employing similar printing

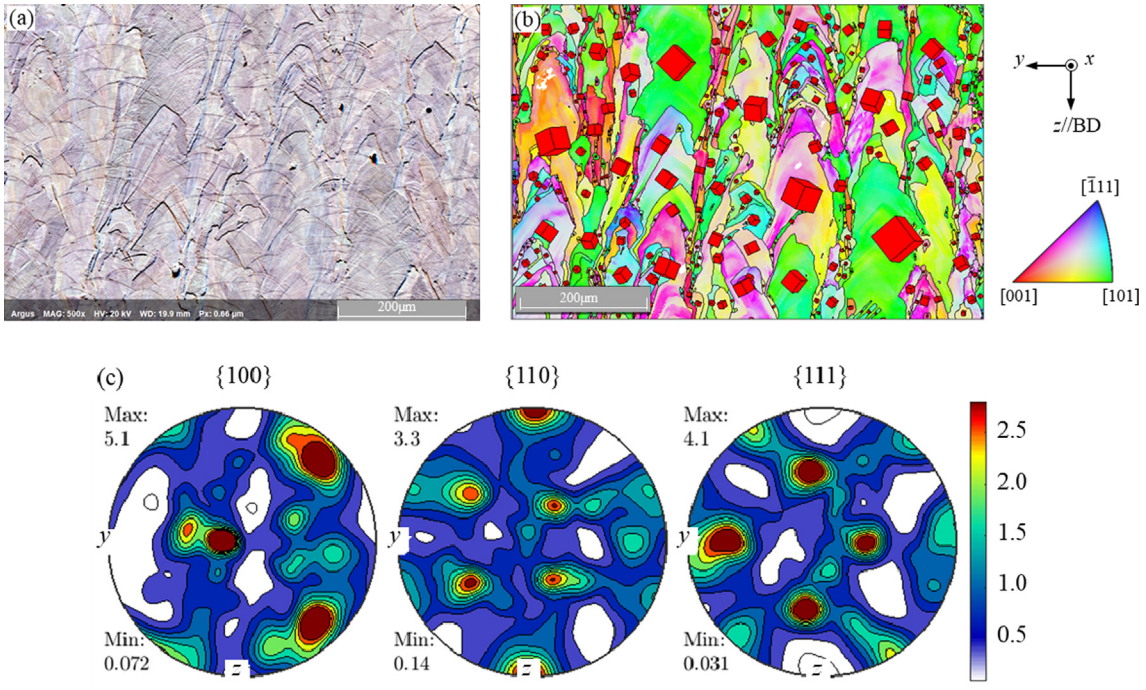

Fig. 13. Typical (a) FSD image, (b) EBSD inverse pole figure maps, with colours presented with respect to the build direction and red cubes showed the crystal orientations of the grains and (c) pole figures of the base metal for the horizontal H1/1 subsample.

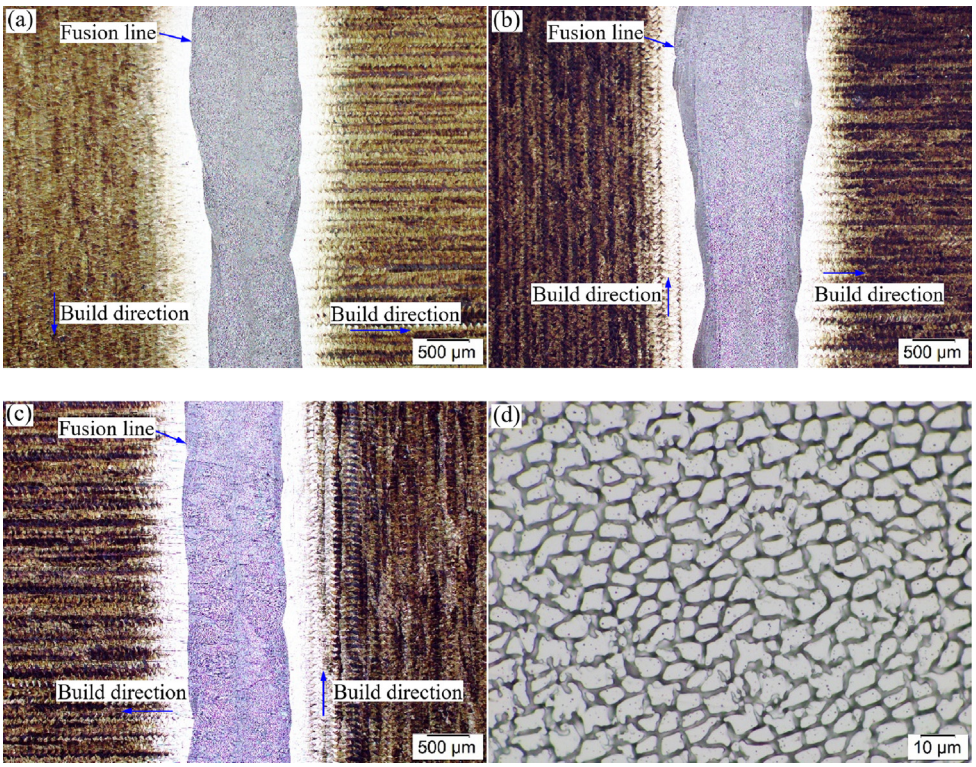

Fig. 14. Typical weld micrographs for the coupon (a) X1/3 (P = 3.5 kW, S = 1750 mm/min), (b) X3/3 (P = 4 kW, S = 1750 mm/min), (c) X4/1 (P = 4 kW, S = 2000 mm/min) and (d) X4/1 (centre of the weld).

parameters [33,80]. The texture and potential phase transformation in laser welds produced with different welding parameters requires further exploration.

4.2.3. Microstructure of laser welded joints

Fig. 14 shows the morphology of the laser weld regions, where the fusion lines and weld centrelines can be clearly observed. The welds are straight and nearly symmetric in shape about the welding path axes, unlike the bead weld profiles in conventional material that has been laser welded [48]. The observed difference in weld shapes is due to the different absorption properties of these two base materials [48]; the higher roughness of the PBF base material results in a higher absorption rate, and therefore a straight and full penetration weld is more likely to form, compared with cold-rolled metallic material.

Under a high-magnification optical microscope, the weld centre was observed to be dominated by equiaxed dendrites (Fig. 14(d)); this morphology results from the low G/R ratio at the weld centre, where G is the temperature gradient and R is the solidification growth rate. Fig. 15 shows typical optical micrographs for the fusion line and weld centre, with the observed microstructure consisting of cellular dendrites, columnar dendrites and equiaxial dendrites. The average grain size in the weld was an order of magnitude larger (~300 μm) than that in the PBF base metal (~28 μm). The large grains exhibited a columnar morphology, with each cell less than 0.5 μm in diameter. The extremely high energy input of laser welding leads to a relatively slow cooling rate, which allows more time for grain coarsening and for the dendrites to propagate further during solidification, potentially leading to reduced strength and ductility in the weld, as discussed in Section 4.4.

The HAZ exhibited a similar microstructure to the PBF base metal. Although the boundaries between the HAZ and the base metal are obscure under an optical microscope, they can be distin-

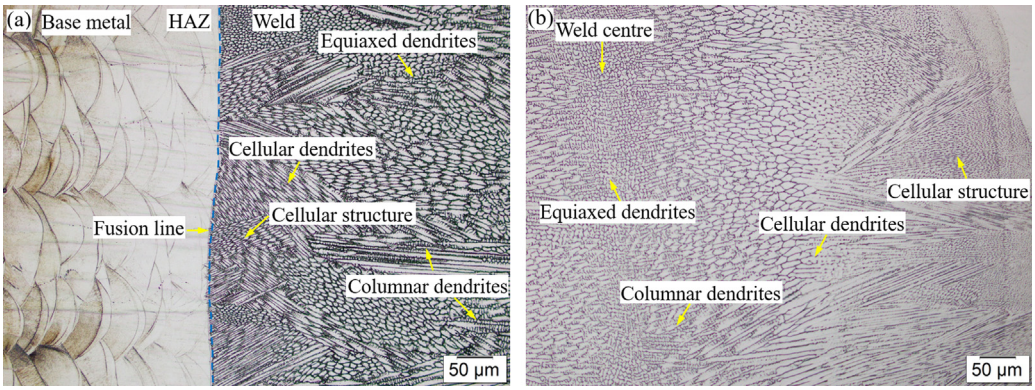

Fig. 15. Typical micrographs at the fusion line, showing (a) the transition zone from base metal to weld and (b) the grain structure of the weld.

guished by the colour change. The average widths of the weld region and HAZ were determined from individual measurements taken at ten uniformly distributed locations across the specimen width. The average measured weld and HAZ widths for all specimens were around 1000 μm and 500 μm respectively. The measured widths of the weld and HAZ are plotted against the energy input of the laser welding in Fig. 16. The weld width increases from 900 μm to 1200 μm and the HAZ width varies from 450 μm to 600 μm, as the energy input increases from 105 J/mm to 137 J/mm. It can therefore be concluded that the PBF 316L base material can be laser welded with narrow weld and HAZ widths, enabling small PBF elements to be mechanically joined to form larger parts.

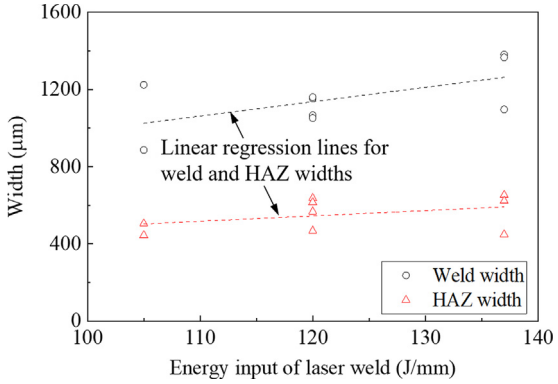

Fig. 16. Variation of the weld and HAZ width with the laser welding energy input.

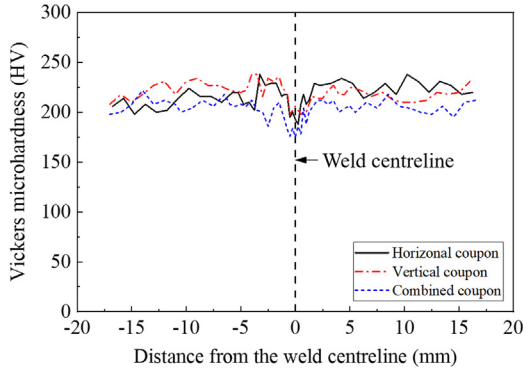

Fig. 17. Variation of microhardness along the longitudinal coupon axis.

4.3. Microhardness

Fig. 17 shows typical microhardness profiles across the laser welded joints in the horizontal, vertical and combined coupons, showing a relatively uniform microhardness profile that reduces at the laser weld. The average microhardness (HV) values for the measurements made in the transverse direction across the coupon width for the weld, HAZ and base metal, are reported in Table 5. The PBF base material had microhardness values between 214 HV and 234 HV, higher than those of conventionally produced counterparts (150 ~ 160 HV) [35]. The adopted build direction was observed to have no significant effect on the microhardness of the PBF 316L base metal, in line with previous studies [29]. The weld was found to have a slightly lower average microhardness (197 HV) than the HAZ (207 HV) and base metal (222 HV), which was also observed in other studies [44,61] and is attributed to the coarser weld microstructure that was described in Section 4.2.3 [35,53].

4.4. Tensile properties and their correlation with microstructure

The stress-strain responses and the key mechanical properties from the tensile coupon tests are presented in this section. The stress-strain responses were determined (i) globally (across the weld, HAZ and base metal), calculated over the parallel length and (ii) locally, within 1 mm long boxes, along the parallel length, capturing separately the properties of the base metal, HAZ and weld regions. The coupons all showed nonlinear stress-strain beha-

Table 5
Summary of the weld, HAZ and base metal microhardness (HV).

Location	H1	H2	H3	V1	V2	V3	X1(H)	X1(V)	X3(H)	X3(V)	X4(H)	X4(V)
Weld	213	243	198	189	178	181	204	204	198	198	181	181
HAZ	196	242	200	203	198	198	220	207	204	212	208	201
Base metal	217	227	227	225	219	214	234	226	218	218	227	216

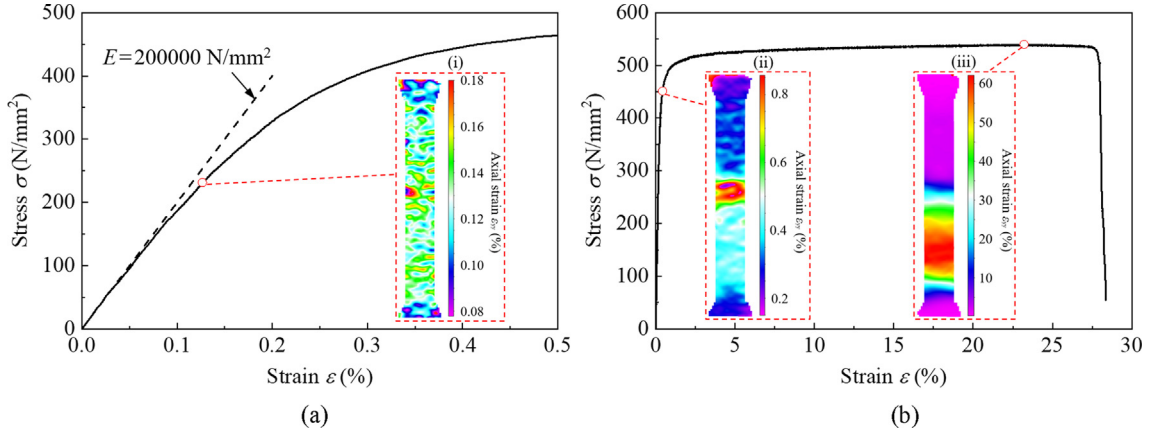

Fig. 18. Measured global stress-strain relationship for the X1/1 tensile coupon showing (a) the initial response and (b) the full response, with DIC axial strain plots at (i) $0.5\sigma_{0.2}$, (ii) $\sigma_{0.2}$ and (iii) σ_u.

viour with gradual material yielding, followed by strain hardening that continued until fracture. Typical global stress-strain curves and single side DIC strain fields at key points during the tensile testing are shown in Figs. 18 and 19 for coupons X1/1 and X3/2 respectively. It can be seen that the X1/1 coupon fractured in the base metal (in the vertical half part), whereas the X3/2 coupon failed in the laser weld. The weld zone is not visible from the DIC strain field until the macroscopic stress level reaches approximately half the 0.2% proof stress (i.e. $0.5\sigma_{0.2}$); beyond this value, the fusion zone exhibits higher local strains than the base metal (under the same load level). The global stress-strain curves are shown in Fig. 20, while the global tensile properties, averaged

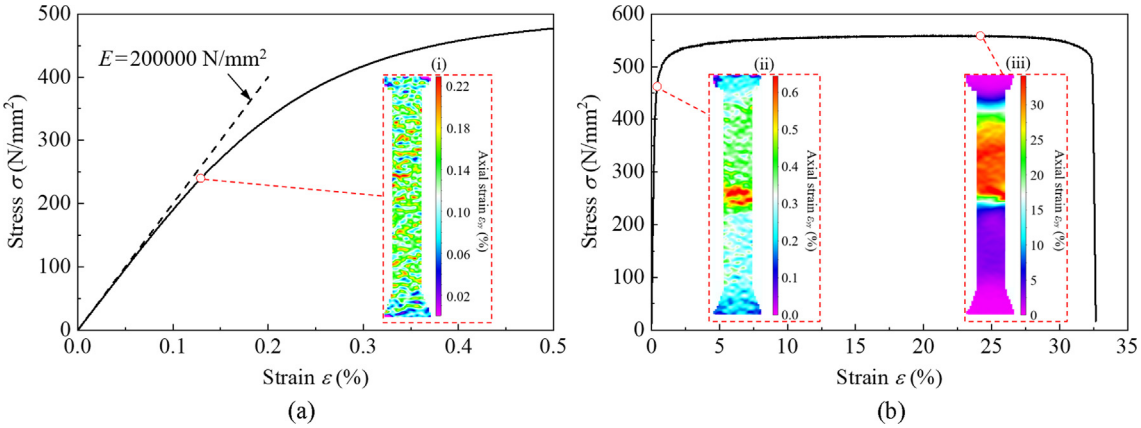

Fig. 19. Measured global stress-strain relationship for the X3/2 tensile coupon showing (a) the initial response and (b) the full response, with DIC axial strain plots at (i) $0.5\sigma_{0.2}$, (ii) $\sigma_{0.2}$ and (iii) σ_u.

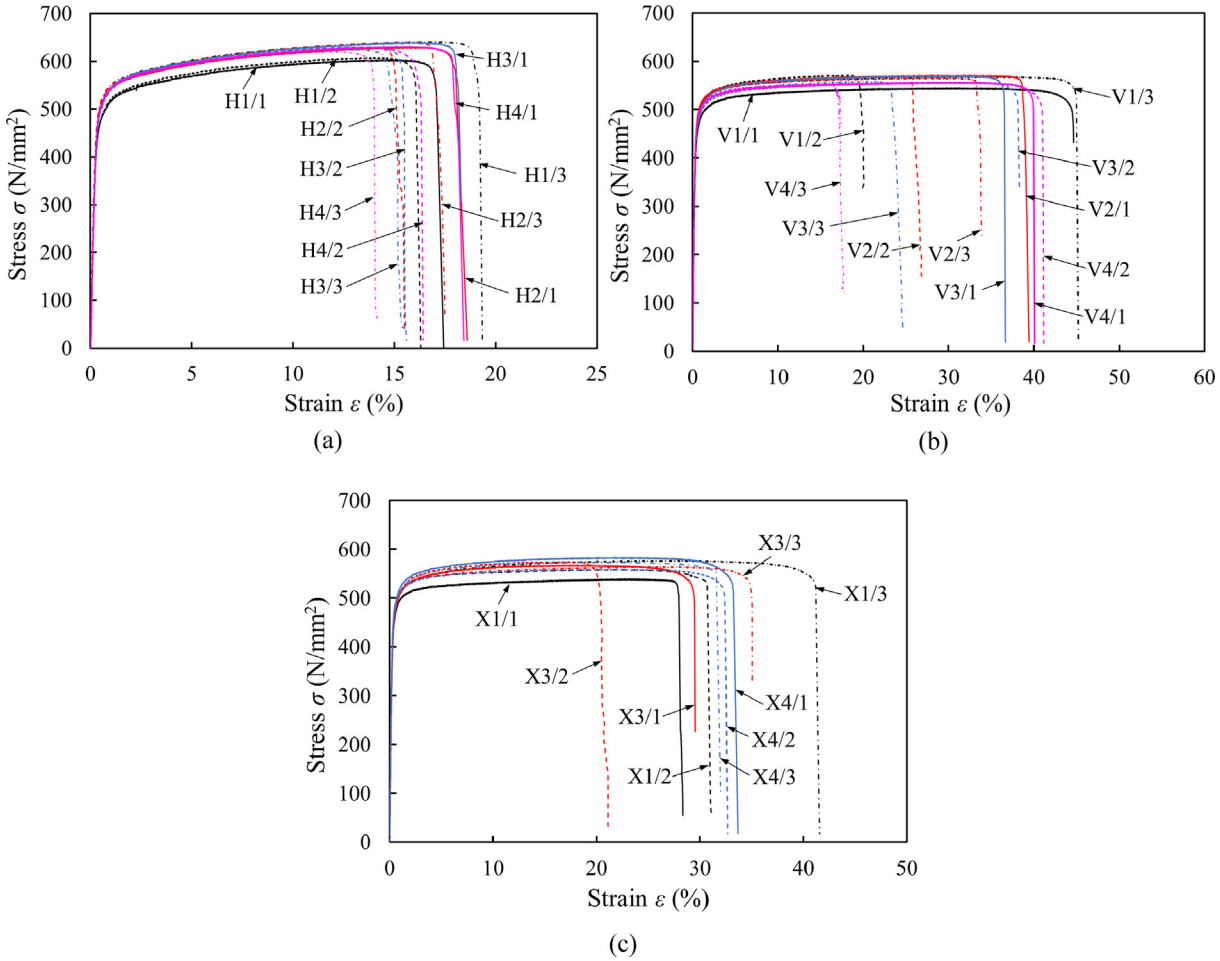

Fig. 20. Global stress-strain curves for the (a) horizontal, (b) vertical and (c) combined tensile coupons.

Table 6
Summary of average global tensile properties from PBF 316L stainless steel coupons with laser welded joints.

Welding parameter family	Coupon type	E (N/mm^2)	$\sigma_{0.2}$ (N/mm^2)	$\sigma_{1.0}$ (N/mm^2)	σ_u (N/mm^2)	$\varepsilon_{u,gl}$ (%)	ε_f (%)	n	$m_{1.0}$	m_u
1	H	194500	480	539	617	15.2	20.3	7.2	3.6	4.0
	V	179400	450	512	561	27.0	39.6	6.1	5.8	7.0
	X	188500	463	515	558	24.6	43.5	6.4	5.8	6.7
2	H	192500	503	555	632	15.3	20.0	7.1	3.3	3.7
	V	184700	459	519	567	27.9	38.7	5.8	5.9	7.2
3	H	193200	490	554	631	14.0	19.3	8.2	3.7	4.1
	V	181800	446	508	561	27.4	38.7	6.2	5.5	6.8
	X	183100	462	521	568	20.5	39.3	7.0	5.4	6.3
4	H	191400	495	553	627	13.6	20.0	7.9	3.5	3.9
	V	177600	451	511	555	24.8	37.3	6.2	6.0	7.1
	X	186000	469	526	571	20.5	42.0	6.5	5.4	6.3

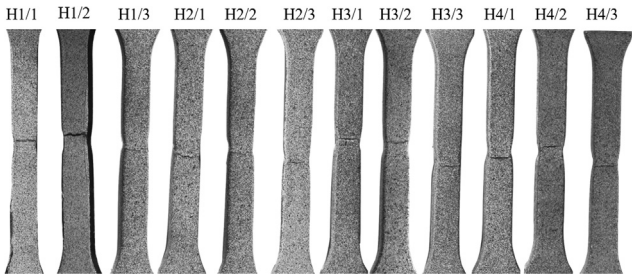

Fig. 21. Horizontal coupons after fracture.

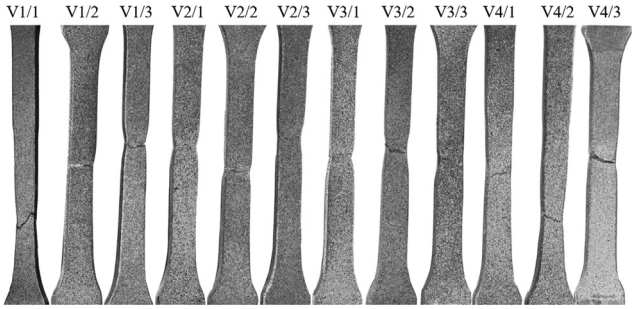

Fig. 22. Vertical coupons after fracture.

per welding parameter and build direction combination, are reported in Table 6; the reported properties are the Young's modulus E, the 0.2% proof strength $\sigma_{0.2}$, the 1.0% proof strength $\sigma_{1.0}$, the ultimate tensile stress σ_u, the average global strain at the ultimate stress over the parallel length $\varepsilon_{u,gl}$, the fracture strain over the marked gauge length ε_f, the Ramberg-Osgood parameter n [81] and the extended parameters $m_{1.0}$ (previously referred to as $n'_{0.2,1.0}$) and m_u (previously referred to as $n'_{0.2,u}$) [82–84]. The Young' modulus E was determined by regression analysis, as described in [8].

Figs. 21-23 show the horizontal, vertical and combined coupons after fracture, respectively. The horizontal specimens fractured in the weld, the vertical specimens fractured either in the base metal (V1/1, V4/1 and V4/2) or in the weld, while the combined specimens all fractured in the base metal of the vertical half parts, except X3/2 which fractured in the weld. The specimens which fractured in the weld generally had a lower fracture strain ($\varepsilon_f \approx 20\%$) compared with the specimens that fractured in the vertical base metal ($\varepsilon_f \approx 40\%$). There is a transition from a cellular microstructure near the PBF base metal to an equiaxed microstructure in the weld centre, where the long cellular or dendrite boundaries and grain boundaries allow cracks to develop more easily with less deformation [49], which leads to a lower fracture strain in the weld than in the vertical base metal. The coupons fractured either at weak points where defects were located or at regions that exhibited a lower ultimate strength. For the vertical and combined coupons, fracture occurred at random positions along the parallel length due to the fact that the weld has a similar ultimate strength to that of the vertical base metal.

Typical engineering stress-strain curves for the horizontal, vertical and combined specimens are shown in Fig. 24, where the local stress-strain responses of the weld, HAZ and base metal are shown. The local stress-strain response is presented in Figs. 25-27 for three

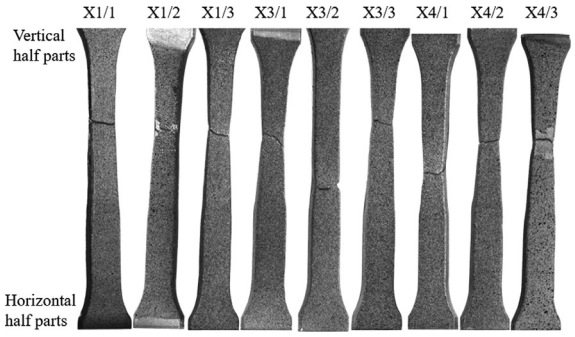

Fig. 23. Combined coupons after fracture.

regions: (i) the centre of the weld, (ii) the centre of the HAZ and (iii) the base metal, away from the fusion line of the weld. Three specimens were tested for each coupon family; the key mechanical properties, averaged per coupon family, as well as the fracture location, are provided in Tables 7-9, where $\varepsilon_{u,gl}$ is the global strain at the ultimate tensile stress. The H and V in the brackets in Table 9 indicate the horizontally and vertically built half parts of the combined specimens. The ultimate tensile stress σ_u and corresponding local strain ε_u are only applicable in the regions where fracture occurred, and are considered as lower bounds for the other two regions.

4.4.1. Comparison with conventionally produced 316L base material

Generally, the PBF 316L base metal had higher proof and ultimate strengths ($\sigma_{0.2}$, $\sigma_{1.0}$ and σ_u) than 316L stainless steel formed by other means [3,85–87], as indicated in Table 10. The increase in

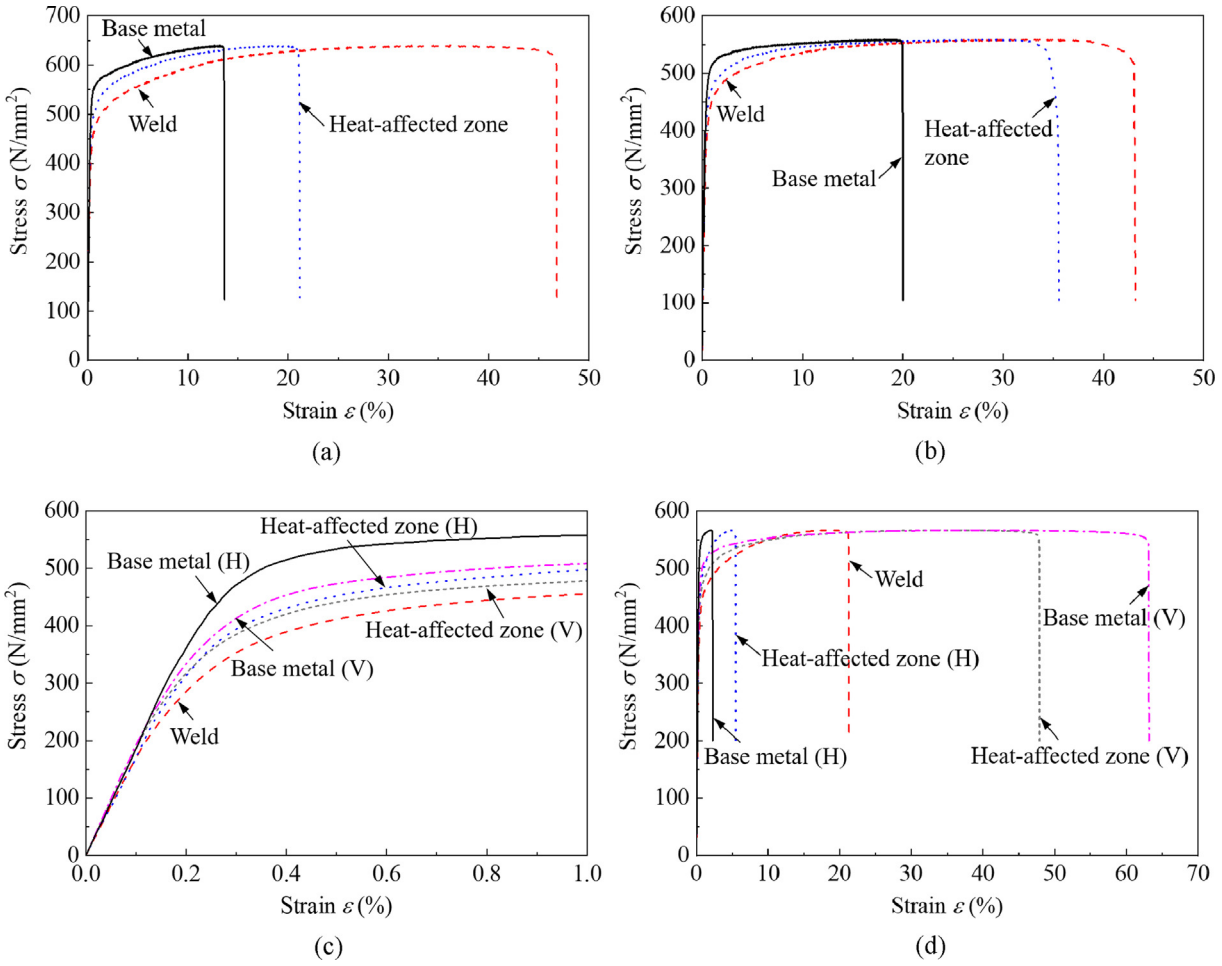

Fig. 24. Typical measured engineering tensile stress-strain curves for a (a) horizontal coupon (H3/1), (b) vertical coupon (V3/3), (c) combined coupon (X3/1, initial response) and (d) combined coupon (X3/1, full response).

ultimate strength σ_u is smaller than that of the 0.2% proof stress $\sigma_{0.2}$. The fracture strain ε_f of the PBF base metal and the conventionally-formed material is similar, while the Young's modulus E of PBF 316L stainless steel is slightly lower than the typically assumed value of E = 200000 N/mm^2 for conventional stainless steel [88]. As previously discussed in Section 4.2, PBF 316L stainless steel has a finer microstructure compared with its conventionally produced counterparts, leading to a higher measured strength, following the Hall-Petch relationship [89,90]. The mechanical properties of the base material within the welded tensile coupons were comparable to the properties reported in the EOS material datasheet (Table 2). It should be noted that there is some scatter in the measured tensile properties of PBF 316L stainless steel among previous studies, in terms of material strengths [24,25] and elongations at fracture [24]. However, PBF 316L stainless steel generally has higher strengths, and comparable or higher ductility relative to conventionally produced 316L stainless steel.

4.4.2. Material anisotropy

The measured material properties of the tested PBF 316L stainless steel exhibited clear anisotropy. The 0.2% proof stress $\sigma_{0.2}$ and ultimate stress σ_u are plotted against the build direction angle θ in Fig. 28, together with existing data from the literature [3,4,18,20,22,24,27–30]. The 0.2% proof stress $\sigma_{0.2}$ and ultimate stress σ_u are observed to decrease with increasing angle θ to the build direction, as shown by the plotted linear regression lines, which matches prior observations [3,4,18,20,22,24,27–30]. Note a regression line cannot be produced for the ultimate stress as none of the horizontal coupons fractured outside the weld in this study.

Previous studies have indicated that epitaxial grain growth due to remelting of the previous layers by the subsequent layers [17,20,26], strong crystallographic texture [8,80] and lack-of-fusion defects [3,20,24,32] may contribute to the observed anisotropy in the mechanical properties. The EBSD map and pole figures in Fig. 13 indicate a weak crystallographic texture in the PBF 316L stainless steel, so the texture is not expected to be the primary cause of the observed mechanical anisotropy. The relative density is deemed to be approaching 100% with very few lack-of-fusion pores observed; hence, the observed material anisotropy is unlikely to stem from lack-of-fusion defects. As reported in Section 4.2, the presence of elongated grains with epitaxial growth following the maximum temperature gradient, parallel to the build direction, indicates the potential correlation between the grain morphology and the exhibited anisotropy. The presence of substructures (such as columnar and equiaxed grains) with acute-angle grain boundaries and finer grain size are two possible causes for the greater measured proof and ultimate strengths of the horizontal specimens when compared to the vertical specimens and vertically built half parts of the combined welded coupons. Previous studies have also reported that fracture strains in horizontal specimens were

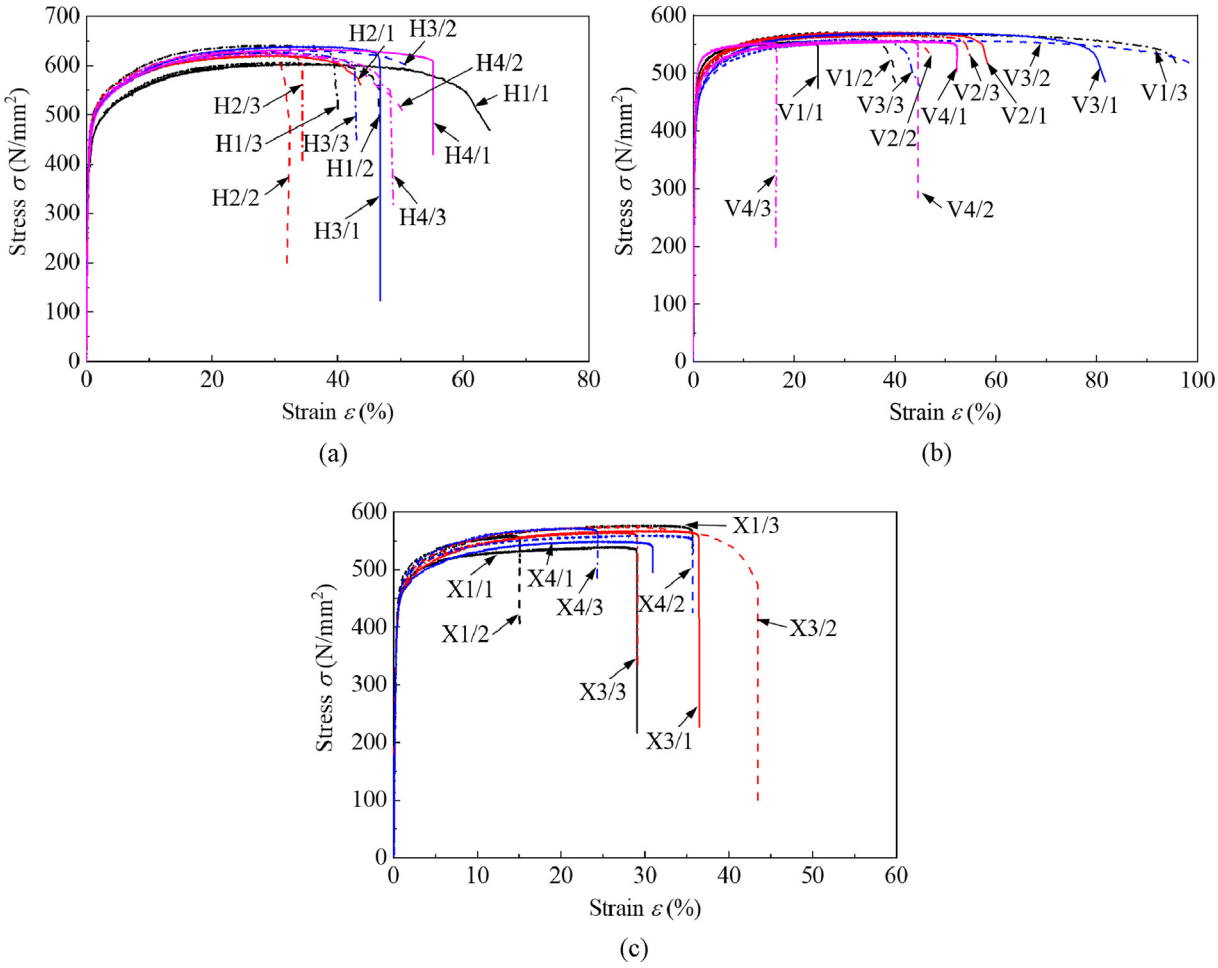

Fig. 25. Measured engineering stress-strain curves for the weld region of the (a) horizontal, (b) vertical and (c) combined tensile coupons.

lower than those in vertical specimens [4]; this may be due to the different mean free paths of dislocations induced by the difference in grain aspect ratio and the orientation of the grain long axes with respect to the loading direction. The vertical specimens exhibited columnar grains parallel to the build direction, as well as the loading direction. The tensile stress was applied perpendicular to the longer axis of the columnar grains for the horizontal specimens. The vertical specimens therefore have more slipping surfaces per unit length than the horizontal specimens. The directional variation of the Young's modulus of steel is related to the crystallographic texture [91,92], associated with the local interatomic potential. For the examined non-textured PBF 316L stainless steel, the anisotropy of the Young's modulus was found to be quite small, which accords with previous studies on austenitic stainless steel [91,92].

4.4.3. Weld properties

The laser welds were observed to have lower 0.2% and 1.0% proof strengths and fracture strains for all the test coupons, compared with the PBF base material. To understand the variation in the 0.2% and 1.0% proof stresses away from the weld centre, typical proof stress distributions along the parallel length of the coupons are presented in Fig. 29. The longitudinal strain fields from one coupon side, prior to fracture, are also provided in Fig. 29, with the largest strain values denoting the fracture locations. For all specimens, the 0.2% and 1.0% proof stresses increase gradually from minimum values in the weld region to steady values in the base metal. For the combined specimens, the lower proof strengths of the vertically built half parts relative to the horizontally built parts, away from the weld region, are clearly visible in Fig. 29 (c). To evaluate the dependency of the energy input on the weld strength, the 0.2% and 1.0% proof stresses of the weld are plotted against the energy input in Fig. 30. The 0.2% and 1.0% proof stresses decrease as the energy input of the laser welding increases; this is due to the grains in the weld and HAZ becoming coarser (as seen in Section 4.2). The results presented in Tables 8 and 9 indicate that the welds had similar ultimate strengths to that of the vertical base metal. Overall, it can be concluded that PBF manufactured parts can be effectively laser welded using suitable welding parameters, but there is a need to consider the potentially lower strength and ductility of the weld compared to the printed base material.

5. Conclusions

Grade 316L stainless steel tensile coupon half parts were manufactured using powder bed fusion (PBF), mechanically joined through laser welding, and tested. The experiments represent a significant expansion of the very limited existing dataset and consider different combinations of build directions. The employed material, manufacturing process and parameters and experimental procedures have been described. Characterisation of the microstructure and mechanical properties has been presented. The PBF 316L base metal revealed a fine cellular microstructure

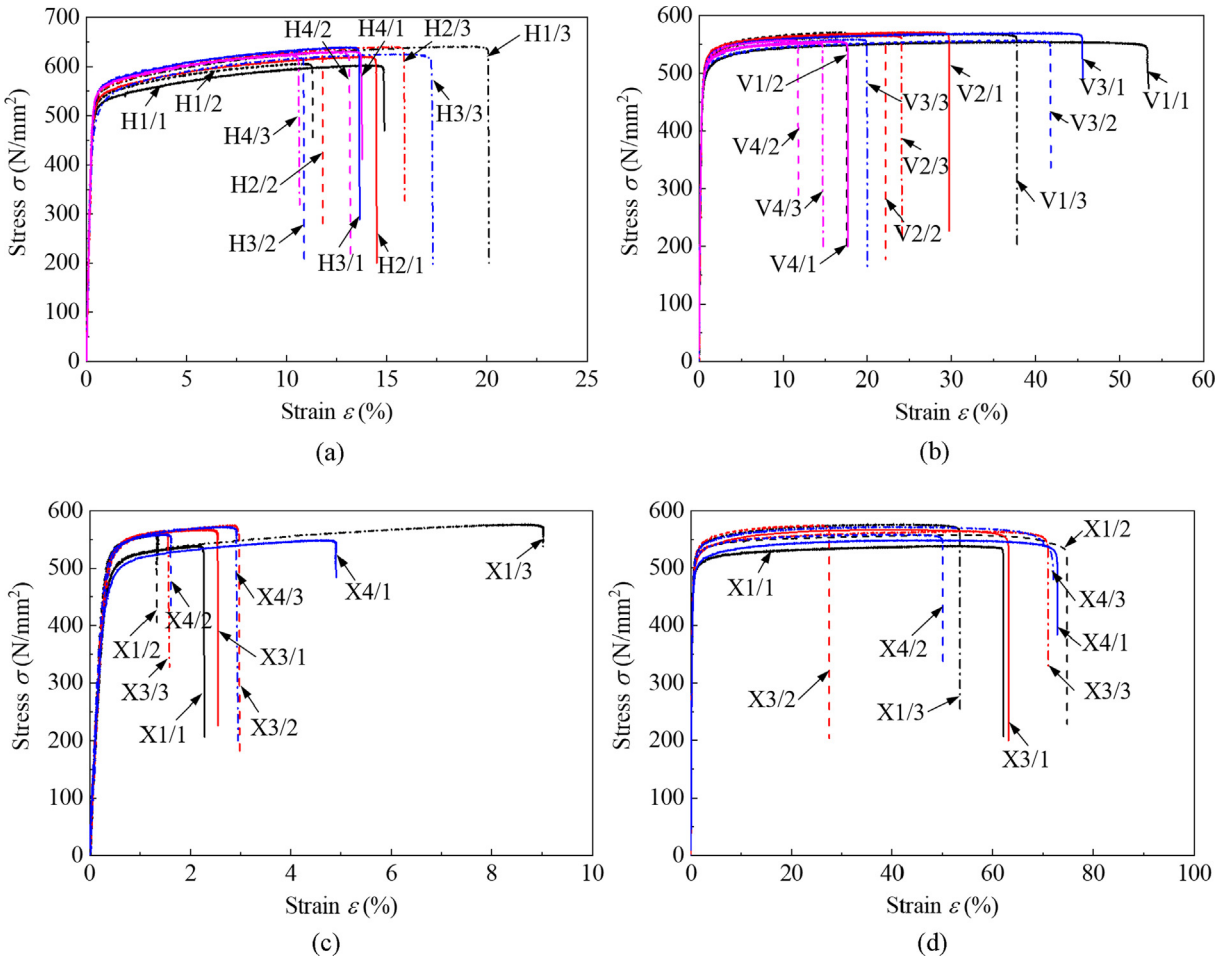

Fig. 26. Measured engineering stress-strain curves for the base metal of the (a) horizontal coupons, (b) vertical coupons, (c) combined coupons (horizontal half parts) and (d) combined coupons (vertical half parts).

and epitaxial grain growth from the remelting zones approximately along the build direction, whereas a combination of equiaxed, columnar and cellular dendritic structures was observed in the laser weld region.

The global and local stress-strain responses of PBF 316L stainless steel with laser welded joints were measured using digital image correlation (DIC). The PBF 316L base material typically had higher proof and ultimate strengths as a result of the finer microstructure, without reduced ductility, but with a lower Young's modulus, when compared with conventionally produced stainless steel. The PBF horizontal base material showed a higher proof stress than the vertical base material; this is attributed to the epitaxial grain growth orientation with respect to the loading direction. The laser weld regions exhibited a lower hardness, proof strength and fracture strain when compared with the PBF base metal, due to the coarser and inhomogeneous microstructure in the weld generated from the high energy laser welding. The widths of the weld and HAZ were observed to be generally narrow and to increase as the energy input of laser welding increased, while the weld strength was observed to decrease. Overall, it has been shown that laser welding could be employed to allow additive manufacturing techniques, such as PBF, to be used to produce large-scale components, such as those used in the construction sector, but, the potentially lower mechanical properties of the welds compared to those of the base metal must be considered in the design process.

CRediT authorship contribution statement

Ruizhi Zhang: Methodology, Software, Formal analysis, Writing - original draft, Visualization, Investigation. **Craig Buchanan:** Methodology, Investigation, Supervision, Writing - review & editing. **Ville-Pekka Matilainen:** Methodology, Investigation. **Dafni Daskalaki-Mountanou:** Methodology, Software, Investigation. **T. Ben Britton:** Methodology, Supervision. **Heidi Piili:** Funding acquisition, Resources, Funding acquisition, Resources. **Antti Salminen:** Funding acquisition, Resources. **Leroy Gardner:** Methodology, Conceptualization, Supervision, Writing - review & editing, Project administration.

Declaration of Competing Interest

The authors declare that they have no known competing financial interests or personal relationships that could have appeared to influence the work reported in this paper.

Acknowledgements

The authors would like to acknowledge the contribution of Gordon Herbert and Paul Crudge for their assistance in the Structural Laboratory at Imperial College London and staff at the LUT Laser Laboratory and machine shop. The authors acknowledge use of

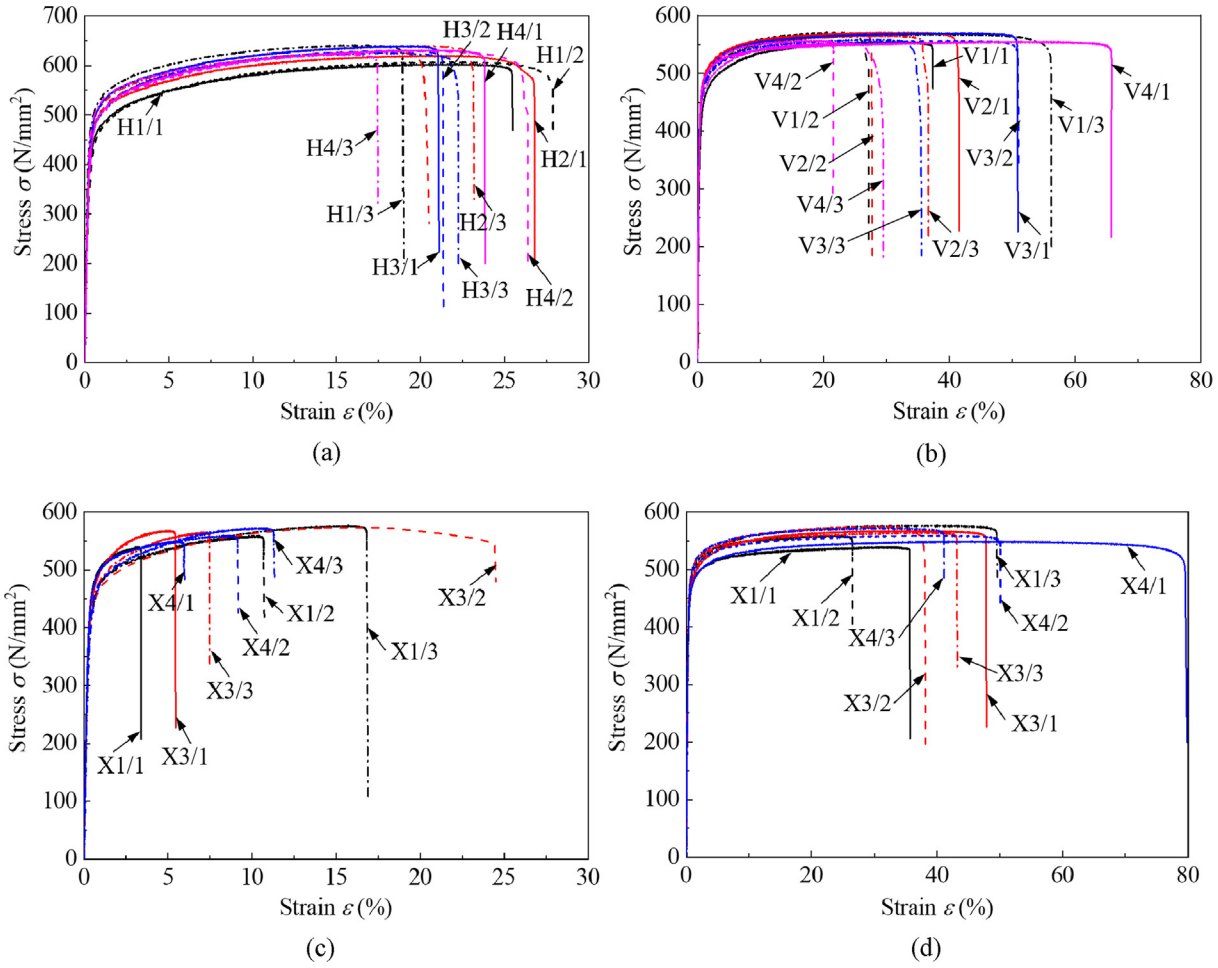

Fig. 27. Measured engineering stress-strain curves for the heat-affected zone (HAZ) of the (a) horizontal coupons, (b) vertical coupons, (c) combined coupons (horizontal half parts) and (d) combined coupons (vertical half parts).

Table 7
Summary of average local tensile properties from the horizontal coupons.

Coupon family name	Fracture location	$\varepsilon_{u,gl}$ (%)	ε_f (%)	Location	E (N/mm^2)	$\sigma_{0.2}$ (N/mm^2)	$\sigma_{1.0}$ (N/mm^2)	σ_u (N/mm^2)	ε_u (%)	n	$m_{1.0}$	m_u
H1	Weld	15.2	20.3	Weld	187900	391	473	608	31.7	5.1	3.8	4.9
				HAZ	201900	429	499	–	–	5.8	3.5	–
				Base metal	206300	502	541	–	–	6.4	2.9	–
H2	Weld	15.3	20.0	Weld	184300	424	505	627	28.1	5.9	4.0	4.9
				HAZ	183200	467	528	–	–	6.6	3.3	–
				Base metal	196900	526	560	–	–	8.7	2.7	–
H3	Weld	14.0	19.3	Weld	174000	426	489	623	32.8	9.0	3.3	4.4
				HAZ	195700	452	514	–	–	6.6	3.1	–
				Base metal	193500	510	556	–	–	8.4	3.1	–
H4	Weld	13.6	20.0	Weld	164600	431	499	627	29.9	8.0	3.5	4.5
				HAZ	180400	459	523	–	–	6.9	3.3	–
				Base metal	192900	537	567	–	–	10.2	2.5	–
Family average	–	14.5	19.9	Weld	177700	418	492	621	30.6	7.0	3.7	4.7
				HAZ	190300	452	516	–	–	6.5	3.3	–
				Base metal	197400	519	556	–	–	8.4	2.8	–

Table 8
Summary of average local tensile properties from the vertical coupons.

Coupon family name	Fracture location	Averaged coupons	$\varepsilon_{u,gl}$ (%)	ε_f (%)	Location	E (N/mm^2)	$\sigma_{0.2}$ (N/mm^2)	$\sigma_{1.0}$ (N/mm^2)	σ_u (N/mm^2)	ε_u (%)	n	$m_{1.0}$	m_u
V1	Base metal	V1/1	31.9	46.8	Weld	164300	397	462	–	–	5.3	4.4	–
					HAZ	169800	399	468	–	–	5.2	4.6	–
					Base metal	173300	453	514	555	50.4	5.1	7.0	7.2
	Weld	V1/2 and V1/3	24.6	36.0	Weld	155800	416	479	562	34.4	6.3	4.5	6.0
					HAZ	159200	420	484	–	–	6.9	4.4	–
					Base metal	171000	467	523	–	–	6.7	6.3	–
V2	Weld	All	27.9	38.7	Weld	173900	404	480	559	37.5	5.0	5.3	7.2
					HAZ	175900	425	490	–	–	5.6	4.9	–
					Base metal	168700	469	521	–	–	7.6	6.3	–
V3	Weld	All	27.4	38.7	Weld	163100	377	448	544	42.1	6.7	4.6	6.4
					HAZ	180000	412	470	–	–	6.8	4.5	–
					Base metal	177500	452	505	–	–	6.8	6.8	–
V4	Base metal	V4/1 and V4/2	29.5	45.0	Weld	163500	400	476	–	–	4.9	5.4	–
					HAZ	172200	432	495	–	–	6.3	5.2	–
					Base metal	175100	471	520	556	65.8	5.5	6.2	6.7
	Weld	V4/3	15.3	22.0	Weld	156500	405	471	552	29.4	5.6	4.5	5.9
					HAZ	196900	401	473	–	–	5.1	4.6	–
					Base metal	177500	462	523	–	–	6.4	7.2	–
Family average	–	–	26.8	38.6	Weld	165700	398	469	554	37.4	5.7	4.9	6.5
					HAZ	174800	418	482	–	–	6.2	4.7	–
					Base metal	177800	462	517	556	60.7	5.4	6.5	6.9

Table 9
Summary of average local tensile properties from the combined coupons.

Coupon family name	Fracture location	Averaged coupons	$\varepsilon_{u,gl}$ (%)	ε_f (%)	Location	E (N/mm^2)	$\sigma_{0.2}$ (N/mm^2)	$\sigma_{1.0}$ (N/mm^2)	σ_u (N/mm^2)	ε_u (%)	n	$m_{1.0}$	m_u
X1	Base metal (V)	All	24.6	43.5	Weld	181300	409	478	–	–	5.4	4.5	–
					HAZ (V)	188000	432	490	–	–	5.8	5.1	–
					HAZ (H)	192400	424	492	–	–	4.8	3.7	–
					Base metal (V)	181200	461	512	553	50.1	6.7	7.2	8.3
					Base metal (H)	202100	501	535	–	–	7.1	2.9	–
X3	Base metal (V)	X3/1 and X3/3	22.0	46.0	Weld	169500	386	459	–	–	5.7	4.1	–
					HAZ (V)	187600	430	488	–	–	6.0	5.0	–
					HAZ (H)	175800	426	493	–	–	6.6	3.0	–
					Base metal (V)	191600	452	509	555	47.3	5.7	6.9	8.1
					Base metal (H)	189700	518	552	–	–	8.5	3.0	–
	Weld	X3/2	17.4	26.0	Weld	183800	416	477	573	27.0	6.3	3.6	4.8
					HAZ (V)	158800	435	494	–	–	8.5	4.3	–
					HAZ (H)	176400	416	479	–	–	7.5	3.4	–
					Base metal (V)	180600	470	530	–	–	6.0	6.3	–
					Base metal (H)	180600	523	560	–	–	7.9	3.4	–
X4	Base metal (V)	All	20.5	42.0	Weld	175800	403	477	–	–	5.1	4.6	–
					HAZ (V)	166900	446	500	–	–	7.2	4.9	–
					HAZ (H)	177100	428	499	–	–	6.0	3.6	–
					Base metal (V)	184700	460	520	563	41.3	5.9	7.2	8.4
					Base metal (H)	179200	516	551	–	–	9.1	3.2	–
Family average	–	–	21.9	41.6	Weld	177100	403	473	573	27.0	5.5	4.4	4.8
					HAZ (V)	177600	437	493	–	–	6.6	4.9	–
					HAZ (H)	181800	425	493	–	–	5.9	3.5	–
					Base metal (V)	184600	460	516	557	46.1	6.1	7.0	8.3
					Base metal (H)	189300	512	547	–	–	8.2	3.1	–

Table 10
Comparison of mechanical properties of conventionally manufactured [3,85–87] and PBF 316L stainless steel from this study.

Reference	Type of 316L stainless steel	E (N/mm^2)	$\sigma_{0.2}$ (N/mm^2)	σ_u (N/mm^2)	ε_f (%)	n
This study	PBF horizontal base metal	179200–206300	501–567	–	–	8.3
	PBF vertical base metal	168700–191700	452–471	553–563	42.0–46.8	5.7
Mower and Long [3]	Wrought	187000	345	563	30.0	–
Yadollahi et al. [85]	Cast	–	262	552	55.0	–
ASTM 473-15 [86]	Forged	–	170	450	40.0	–
EN 10088-2 [87]	Hot-rolled	193000	220	530–680	40.0	–
	Cold-rolled	193000	240	530–680	40.0	–

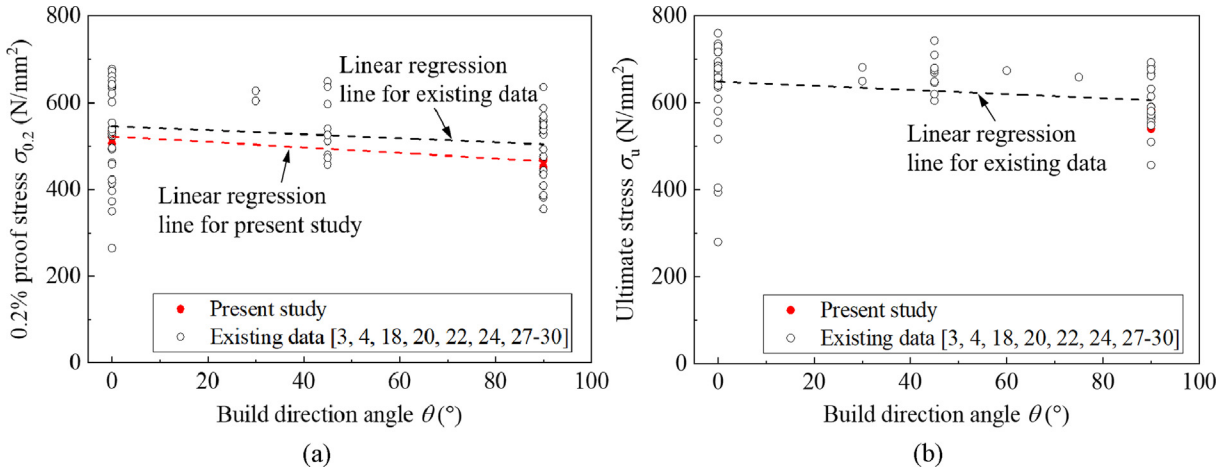

Fig. 28. Variation of the (a) 0.2% proof stress $\sigma_{0.2}$ and (b) ultimate stress σ_u with the build direction angle for the PBF base metal.

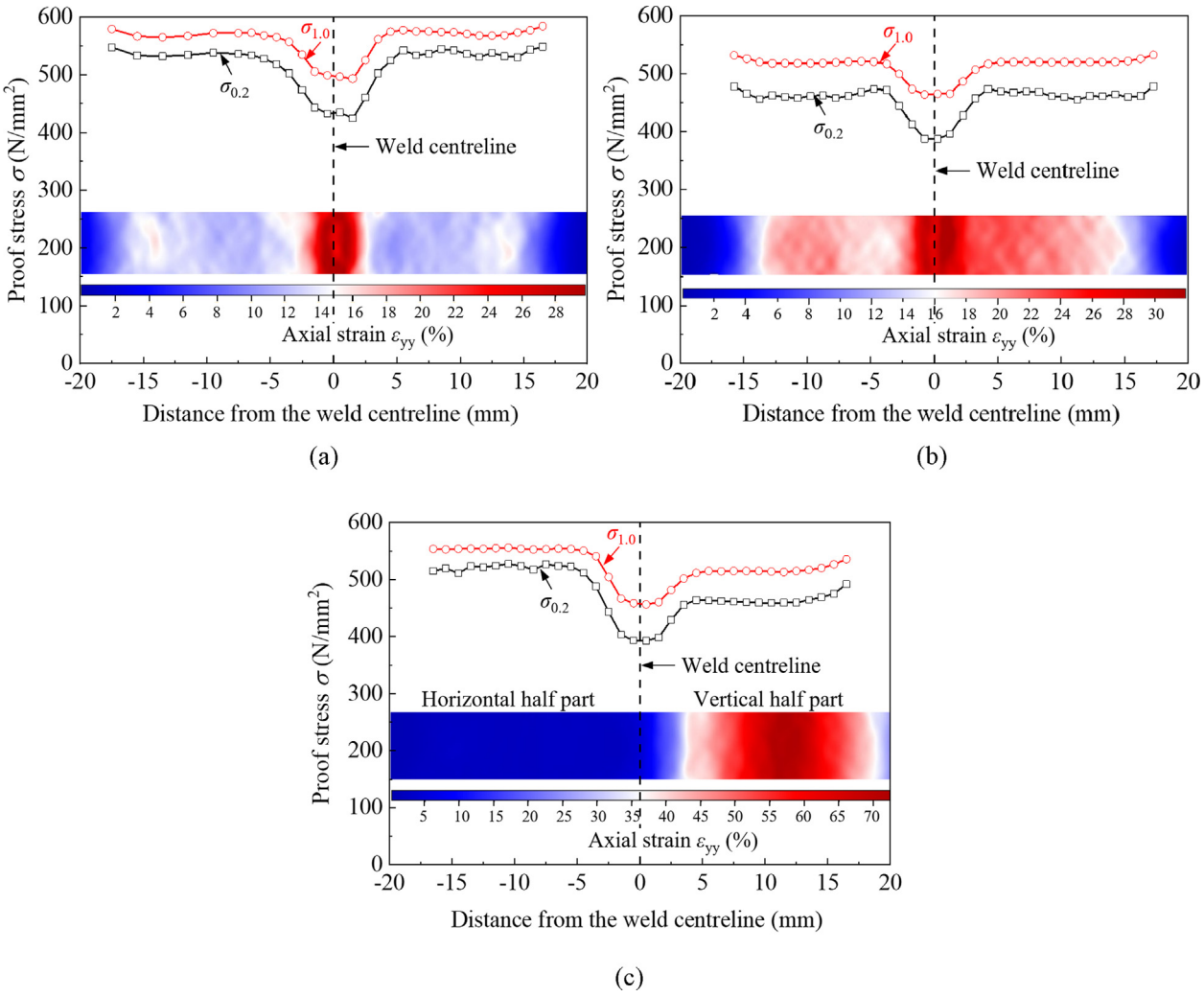

Fig. 29. Variation in the 0.2% and 1.0% proof stresses moving away from the weld centre for typical (a) horizontal (H3/1), (b) vertical (V3/3) and (c) combined (X3/1) tensile coupons.

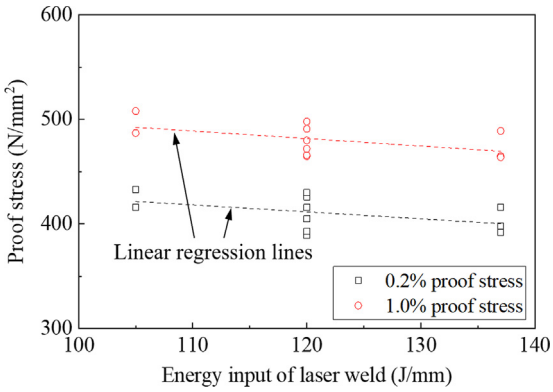

Fig. 30. Variation of the weld strength with the laser welding energy input.

characterisation facilities within the Harvey Flower Electron Microscopy Suite in the Department of Materials at Imperial College London. The authors also gratefully acknowledge the China Scholarship Council for its financial support.

References

[1] CEN (European Committee for Standardization) (2017). Additive manufacturing—General principles—Terminology. EN ISO 52900:2017, Brussels.
[2] W.E. Frazier, Metal additive manufacturing: A review, J. Mater. Eng. Perform. 23 (6) (2014) 1917–1928.
[3] T.M. Mower, M.J. Long, Mechanical behaviour of additive manufactured, powder-bed laser-fused materials, Mater. Sci. Eng., A 651 (2016) 198–213.
[4] C. Buchanan, V.P. Matilainen, A. Salminen, L. Gardner, Structural performance of additive manufactured metallic material and cross-sections, J. Constr. Steel Res. 136 (2017) 35–48.
[5] M.O. John, Photo-glyph recording. U.S. Patent No. 2,775,758. Washington, DC (1956).
[6] L. Gardner, P. Kyvelou, G. Herbert, C. Buchanan, Testing and initial verification of the world's first metal 3D printed bridge, J. Constr. Steel Res. 172 (2020) 106233.
[7] C. Buchanan, L. Gardner, Metal 3D printing in construction: A review of methods, research, applications, opportunities and challenges, Eng. Struct. 180 (2019) 332–348.
[8] P. Kyvelou, H. Slack, D.D. Mountanou, M.A. Wadee, T.B. Britton, C. Buchanan, L. Gardner, Mechanical and microstructural testing of wire and arc additively manufactured sheet material, Mater. Des. 192 (2020) 108675.
[9] J.J. Yan, M.T. Chen, W.M. Quach, M. Yan, B. Young, Mechanical properties and cross-sectional behavior of additively manufactured high strength steel tubular sections, Thin-Walled Struct. 144 (2019) 106158.
[10] M. Ashraf, I. Gibson, M.G. Rashed, Challenges and prospects of 3d printing in structural engineering, Space and Composite Structures, Perth, 2018.
[11] R. Zhang, L. Gardner, C. Buchanan, V.P. Matilainen, H. Piili, A. Salminen, Testing and analysis of additively manufactured stainless steel CHS in compression, Thin-Walled Struct. 159 (2021) 107270.
[12] L.P. Lam, D.Q. Zhang, Z.H. Liu, C.K. Chua, Phase analysis and microstructure characterisation of AlSi10Mg parts produced by selective laser melting, Virtual Phys. Prototyping 10 (4) (2015) 207–215.
[13] I. Rosenthal, A. Stern, N. Frage, Microstructure and mechanical properties of AlSi10Mg parts produced by the laser beam additive manufacturing (AM) technology, Metall. Microstruct. Anal. 3 (6) (2014) 448–453.
[14] Y. Idell, C. Campbell, L. Levine, F. Zhang, G. Olson, D. Snyder, Characterization of nickel-based superalloys processed through direct metal laser sintering technique of additive manufacturing, Microsc. Microanal. 21 (S3) (2015) 465–466.
[15] T. Vilaro, C. Colin, J.D. Bartout, L. Nazé, M. Sennour, Microstructural and mechanical approaches of the selective laser melting process applied to a nickel-base superalloy, Mater. Sci. Eng., A 534 (2012) 446–451.
[16] C. Pleass, S. Jothi, Influence of powder characteristics and additive manufacturing process parameters on the microstructure and mechanical behaviour of Inconel 625 fabricated by selective laser melting, Addit. Manuf. 24 (2018) 419–431.
[17] M. Montero Sistiaga, S. Nardone, C. Hautfenne, J. Van Humbeeck, Effect of heat treatment of 316L stainless steel produced by selective laser melting (SLM), in: Proceedings of the 27th Annual International Solid Freeform Fabrication Symposium-An Additive Manufacturing Conference, 2016, pp. 558–565.
[18] H.H. Alsalla, C. Smith, L. Hao, Effect of build orientation on the surface quality, microstructure and mechanical properties of selective laser melting 316L stainless steel, Rapid Prototyping J. 24 (1) (2018) 9–17.
[19] J.R. Trelewicz, G.P. Halada, O.K. Donaldson, G. Manogharan, Microstructure and corrosion resistance of laser additively manufactured 316L stainless steel, JOM 68 (3) (2016) 850–859.
[20] A. Mertens, S. Reginster, Q. Contrepois, T. Dormal, O. Lemaire, J. Lecomte-Beckers, Microstructures and mechanical properties of stainless steel AISI 316L processed by selective laser melting, Mater. Sci. Forum 783 (2014) 898–903.
[21] M. Ghasri-Khouzani, H. Peng, R. Attardo, P. Ostiguy, J. Neidig, R. Billo, D. Hoelzle, M.R. Shankar, Direct metal laser-sintered stainless steel: Comparison of microstructure and hardness between different planes, Int. J. Adv. Manuf. Technol. 95 (9–12) (2018) 4031–4037.
[22] E. Liverani, S. Toschi, L. Ceschini, A. Fortunato, Effect of selective laser melting (SLM) process parameters on microstructure and mechanical properties of 316L austenitic stainless steel, J. Mater. Process. Technol. 249 (2017) 255–263.
[23] J. Suryawanshi, K.G. Prashanth, U. Ramamurty, Mechanical behavior of selective laser melted 316L stainless steel, Mater. Sci. Eng., A 696 (2017) 113–121.
[24] R. Casati, J. Lemke, M. Vedani, Microstructure and fracture behaviour of 316L austenitic stainless steel produced by selective laser melting, J. Mater. Sci. Technol. 32 (8) (2016) 738–744.
[25] D. Wang, C. Song, Y. Yang, Y. Bai, Investigation of crystal growth mechanism during selective laser melting and mechanical property characterization of 316L stainless steel parts, Mater. Des. 100 (2016) 291–299.
[26] A. Leicht, U. Klement, E. Hryha, Effect of build geometry on the microstructural development of 316L parts produced by additive manufacturing, Mater. Charact. 143 (2018) 137–143.
[27] S. Wen, S. Li, Q. Wei, C. Yan, S. Zhang, Y. Shi, Effect of molten pool boundaries on the mechanical properties of selective laser melting parts, J. Mater. Process. Technol. 214 (11) (2014) 2660–2667.
[28] H. Meier, C. Haberland, Experimental studies on selective laser melting of metallic parts, Mater. Sci. Eng. Technol. 39 (9) (2008) 665–670.
[29] I. Tolosa, F. Garciandía, F. Zubiri, F. Zapirain, A. Esnaola, Study of mechanical properties of AISI 316 stainless steel processed by "selective laser melting", following different manufacturing strategies, Int. J. Adv. Manuf. Technol. 51 (5–8) (2010) 639–647.
[30] A.B. Spierings, N. Herres, G. Levy, Influence of the particle size distribution on surface quality and mechanical properties in AM steel parts, Rapid Prototyping J. 17 (3) (2011) 195–202.
[31] E. Yasa, J.P. Kruth, Microstructural investigation of Selective Laser Melting 316L stainless steel parts exposed to laser re-melting, Procedia Eng. 19 (2011) 389–395.
[32] M. Zhang, C.N. Sun, X. Zhang, P.C. Goh, J. Wei, D. Hardacre, H. Li, Fatigue and fracture behaviour of laser powder bed fusion stainless steel 316L: Influence of processing parameters, Mater. Sci. Eng., A 703 (2017) 251–261.
[33] H. Choo, K.L. Sham, J. Bohling, A. Ngo, X. Xiao, Y. Ren, P.J. Depond, M.J. Matthews, E. Garlea, Effect of laser power on defect, texture, and microstructure of a laser powder bed fusion processed 316L stainless steel, Mater. Des. 164 (2019) 107534.
[34] A. AlFaify, J. Hughes, K. Ridgway, Controlling the porosity of 316L stainless steel parts manufactured via the powder bed fusion process, Rapid Prototyping J. 25 (1) (2019) 162–175.
[35] Z. Sun, X. Tan, S.B. Tor, W.Y. Yeong, Selective laser melting of stainless steel 316L with low porosity and high build rates, Mater. Des. 104 (2016) 197–204.
[36] D. Kianersi, A. Mostafaei, A.A. Amadeh, Resistance spot welding joints of AISI 316L austenitic stainless steel sheets: Phase transformations, mechanical properties and microstructure characterizations, Mater. Des. 61 (2014) 251–263.
[37] Adira. http://www.adira.pt/002.aspx?dqa=0:0:0:42:0:0:-1:0:0&ct=46
[38] R.E.C.E.P. Gümrük, R.A.W. Mines, Compressive behaviour of stainless steel micro-lattice structures, Int. J. Mech. Sci. 68 (2013) 125–139.
[39] Y. Ibrahim, C.M. Davies, C. Maharaj, Z. Li, J.P. Dear, P.A. Hooper, Post-yield performance of additive manufactured cellular lattice structures, Prog. Addit. Manuf. (2020) 1–10.
[40] Z. Xiao, Y. Yang, R. Xiao, Y. Bai, C. Song, D. Wang, Evaluation of topology-optimized lattice structures manufactured via selective laser melting, Mater. Des. 143 (2018) 27–37.
[41] L. Zhang, B. Song, A. Zhao, R. Liu, L. Yang, Y. Shi, Study on mechanical properties of honeycomb pentamode structures fabricated by laser additive manufacturing: Numerical simulation and experimental verification, Compos. Struct. 226 (2019) 111199.
[42] J. Xiong, D. Gu, H. Chen, D. Dai, Q. Shi, Structural optimization of re-entrant negative Poisson's ratio structure fabricated by selective laser melting, Mater. Des. 120 (2017) 307–316.
[43] S. Galjaard, S. Hofman, N. Perry, S. Ren, Optimizing structural building elements in metal by using additive manufacturing. In Proceedings of the International Association for Shell and Spatial Structures (IASS) Symposia 2015, Amsterdam (2015).
[44] G. Casalino, S.L. Campanelli, A.D. Ludovico, Laser-arc hybrid welding of wrought to selective laser molten stainless steel, Int. J. Adv. Manuf. Technol. 68 (1–4) (2013) 209–216.
[45] Y. Feng, Z. Luo, Z. Liu, Y. Li, Y. Luo, Y. Huang, Keyhole gas tungsten arc welding of AISI 316L stainless steel, Mater. Des. 85 (2015) 24–31.
[46] F. Muhammad, A. Ahmad, A. Farooq, W. Haider, Effect of post-weld heat treatment on mechanical and electrochemical properties of gas metal arc-welded 316L (X2CrNiMo 17–13-2) stainless steel, J. Mater. Eng. Perform. 25 (10) (2016) 4283–4291.

[47] B. Kocabekir, R. Kacar, S. Gündüz, F. Hayat, An effect of heat input, weld atmosphere and weld cooling conditions on the resistance spot weldability of 316L austenitic stainless steel, J. Mater. Process. Technol. 195 (1–3) (2008) 327–335.
[48] V.P. Matilainen, J. Pekkarinen, A. Salminen, Weldability of additive manufactured stainless steel, Physics Procedia 83 (2016) 808–817.
[49] S.C. Tjong, S.M. Zhu, N.J. Ho, J.S. Ku, Microstructural characteristics and creep rupture behavior of electron beam and laser welded AISI 316L stainless steel, J. Nucl. Mater. 227 (1–2) (1995) 24–31.
[50] L. Gardner, Y. Bu, M. Theofanous, Laser-welded stainless steel I-sections: residual stress measurements and column buckling tests, Eng. Struct. 127 (2016) 536–548.
[51] Y. Bu, L. Gardner, Laser-welded stainless steel I-section beam-columns: testing, simulation and design, Eng. Struct. 179 (2019) 23–36.
[52] R.M. Molak, K. Paradowski, T. Brynk, L. Ciupinski, Z. Pakiela, K.J. Kurzydlowski, Measurement of mechanical properties in a 316L stainless steel welded joint, Int. J. Press. Vessels Pip. 86 (2009) 43–47.
[53] V.A. Ventrella, J.R. Berretta, W. De Rossi, Pulsed Nd: YAG laser seam welding of AISI 316L stainless steel thin foils, J. Mater. Process. Technol. 210 (14) (2010) 1838–1843.
[54] K. Furuya, M. Ida, M. Miyashita, H. Nakamura, Mechanical properties of F82H/316L and 316L/316L welds upon the target back-plate of IFMIF, J. Nucl. Mater. 386 (2009) 963–966.
[55] J. Kell, J.R. Tyrer, R.L. Higginson, R.C. Thomson, Microstructural characterization of autogenous laser welds on 316L stainless steel using EBSD and EDS, J. Microsc. 217 (2) (2005) 167–173.
[56] Y. Li, S. Hu, J. Shen, B. Hu, Dissimilar welding of H62 brass-316L stainless steel using continuous-wave Nd: YAG laser, Mater. Manuf. Processes 29 (8) (2014) 916–921.
[57] I. Tomashchuk, D. Grevey, P. Sallamand, Dissimilar laser welding of AISI 316L stainless steel to Ti6-Al4-6V alloy via pure vanadium interlayer, Mater. Sci. Eng., A 622 (2015) 37–45.
[58] S. Chen, M. Zhang, J. Huang, C. Cui, H. Zhang, X. Zhao, Microstructures and mechanical property of laser butt welding of titanium alloy to stainless steel, Mater. Des. 53 (2014) 504–511.
[59] A.P. Reynolds, F. Duvall, Digital image correlation for determination of weld and base metal constitutive behaviour, Welding Res. Supple. 78 (1999) 355–360.
[60] B.L. Boyce, P.L. Reu, C.V. Robino, The constitutive behaviour of laser welds in 304L stainless steel determined by digital image correlation, Metallur. Mater. Trans. A 37 (8) (2006) 2481–2492.
[61] M. Rossini, P.R. Spena, L. Cortese, P. Matteis, D. Firrao, Investigation on dissimilar laser welding of advanced high strength steel sheets for the automotive industry, Mater. Sci. Eng., A 628 (2015) 288–296.
[62] C. Leitão, I. Galvão, R.M. Leal, D.M. Rodrigues, Determination of local constitutive properties of aluminium friction stir welds using digital image correlation, Mater. Des. 33 (2012) 69–74.
[63] M. Harraz, N. El-Mahallawy, K. Abd Elghany, M. Schleser, H. Palkowski, A. Klingner, Characterization of 3D printed stainless steel SS316L powders joined by TIG-, plasma- and laser welding, J. Eng. Sci. Mil. Technol. 1 (2) (2017) 91–95.
[64] B. He, X.J. Tian, X. Cheng, J. Li, H.M. Wang, Effect of weld repair on microstructure and mechanical properties of laser additive manufactured Ti-55511 alloy, Mater. Des. 119 (2017) 437–445.
[65] H. Yu, F. Li, J. Yang, J. Shao, Z. Wang, X. Zeng, Investigation on laser welding of selective laser melted Ti-6Al-4V parts: Weldability, microstructure and mechanical properties, Mater. Sci. Eng., A 712 (2018) 20–27.
[66] C. Zhang, Y. Bao, H. Zhu, X. Nie, W. Zhang, S. Zhang, X. Zeng, A comparison between laser and TIG welding of selective laser melted AlSi10Mg, Opt. Laser Technol. 120 (2019) 105696.
[67] X. Chen, J. Zhang, X. Chen, X. Cheng, Z. Huang, Electron beam welding of laser additive manufacturing Ti–6.5Al–3.5Mo–1.5Zr–0.3Si titanium alloy thick plate, Vacuum 151 (2018) 116–121.
[68] J. Yang, Y. Wang, F. Li, W. Huang, G. Jing, Z. Wang, X. Zeng, Weldability, microstructure and mechanical properties of laser-welded selective laser melted 304 stainless steel joints, J. Mater. Sci. Technol. 35 (9) (2019) 1817–1824.
[69] EOS (2014). Material data sheet EOS stainless steel 316L.
[70] CEN (European Committee for Standardization). (2016). Metallic materials - Tensile testing - Part 1: Method of test at room temperature. EN ISO 6892-1: 2016, Brussels.
[71] ASTM, Standard Guide for Preparation of Metallographic Specimens. *ASTM E3–11:2017*, International (American Society for Testing and Materials), West Conshohocken, PA, 2017.
[72] W.S. Rasband, ImageJ National Institutes of Health, Bethesda, Maryland.
[73] S.M. Yusuf, Y. Chen, R. Boardman, S. Yang, N. Gao, Investigation on Porosity and Microhardness of 316L Stainless Steel Fabricated by Selective Laser Melting, Metals 7 (2) (2017) 64.
[74] ASTM International (American Society for Testing and Materials), Standard Practice for Microetching Metals and Alloys, ASTM E407–07:2007, West Conshohocken, PA, 2007.
[75] CEN (European Committee for Standardization) (2018). Metallic materials - Vickers hardness test - Part 1: Test method. EN ISO 6507-1:2018, Brussels.
[76] LaVision, Davis 8(4) (2017).
[77] D. Tomus, Y. Tian, P.A. Rometsch, M. Heilmaier, X. Wu, Influence of post heat treatments on anisotropy of mechanical behaviour and microstructure of Hastelloy-X parts produced by selective laser melting, Mater. Sci. Eng., A 667 (2016) 42–53.
[78] D. Gu, Y. Shen, Processing conditions and microstructural features of porous 316L stainless steel components by DMLS, Appl. Surf. Sci. 255 (5) (2008) 1880–1887.
[79] S.L. Campanelli, G. Casalino, N. Contuzzi, A. Angelastro, A.D. Ludovico, Analysis of the molten/solidified zone in selective laser melted parts, High-Power Laser Materials Processing: Lasers, Beam Delivery, Diagnostics, and Applications III, International Society for Optics and Photonics, 2014.
[80] T. Niendorf, S. Leuders, A. Riemer, H.A. Richard, T. Tröster, D. Schwarze, Highly anisotropic steel processed by selective laser melting, Metall. Mater. Trans. B 44 (4) (2013) 794–796.
[81] W. Ramberg, W.R. Osgood, Description of stress-strain curves by three parameters (1943).
[82] E. Mirambell, E. Real, On the calculation of deflections in structural stainless steel beams: An experimental and numerical investigation, J. Constr. Steel Res. 54 (1) (2000) 109–133.
[83] K.J. Rasmussen, Full-range stress-strain curves for stainless steel alloys, J. Constr. Steel Res. 59 (1) (2003) 47–61.
[84] L. Gardner, M. Ashraf, Structural design for non-linear metallic materials, Eng. Struct. 28 (6) (2006) 926–934.
[85] A. Yadollahi, N. Shamsaei, S.M. Thompson, D.W. Seely, Effects of process time interval and heat treatment on the mechanical and microstructural properties of direct laser deposited 316L stainless steel, Mater. Sci. Eng., A 644 (2015) 171–183.
[86] ASTM A473-15. Standard Specification for Stainless Steel Forgings, pp. 1-5.
[87] CEN (European Committee for Standardization) (2005). Stainless steels – Part 2: Technical delivery conditions for sheet/plate and strip of corrosion resisting steels for general purposes. EN 10088-2:2005, Brussels.
[88] I. Arrayago, E. Real, L. Gardner, Description of strain curves for stainless steel alloys, Mater. Des. 87 (2015) 540–552.
[89] E.O. Hall, The Deformation and Ageing of Mild Steel: III Discussion of Results, Proc. Phys. Soc. London, Sect. B 64 (9) (1951) 747.
[90] N.J. Petch, The cleavage strength of polycrystals, J. Iron Steel Inst. 174 (1953) 25–28.
[91] H.M. Ledbetter, Monocrystal-polycrystal elastic constants of a stainless steel, Phys. Status Solidi A 85 (1) (1984) 89–96.
[92] H.M. Ledbetter, N.V. Frederick, M.W. Austin, Elastic-constant variability in stainless-steel 304, J. Appl. Phys. 51 (1) (1980) 305–309.